

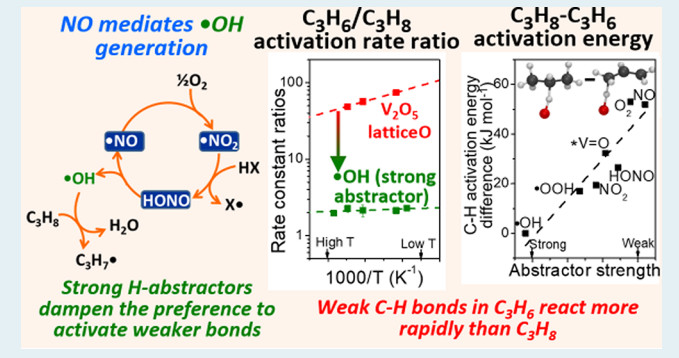
#### Selective C-H Bond Activation via NO<sub>x</sub>-Mediated Generation of **Strong H-Abstractors**

Leelavathi Annamalai, Yilang Liu, and Prashant Deshlahra\*

Department of Chemical and Biological Engineering, Tufts University, Medford, Massachusetts 02155, United States

Supporting Information

ABSTRACT: Mechanistic details and product distributions for C<sub>3</sub>H<sub>8</sub>-O<sub>2</sub> reactions catalyzed by gas-phase NO<sub>x</sub> species are compared to reactions on solid V<sub>2</sub>O<sub>5</sub> catalysts. C<sub>3</sub>H<sub>8</sub> conversions are greatly enhanced by addition of small concentrations of NO to C<sub>3</sub>H<sub>8</sub>-O<sub>2</sub> mixtures without solid catalysts because homogeneous catalytic redox cycles involving oxidation of NO to NO2, reduction by H-addition to form HONO and release of OH radicals facilitate abstraction of H-atoms from strong C-H bonds in C<sub>3</sub>H<sub>8</sub>. NO<sub>x</sub>-mediated conversions exhibit C<sub>3</sub>H<sub>6</sub> selectivity values among the highest reported at similar oxidative conditions because OH radicals are strong abstractors that activate C-H bonds via early transition states that do not exhibit significant



bond elongation, which dampens bond-strength sensitivity and the preference to activate weak allylic C-H bonds in C<sub>3</sub>H<sub>6</sub> products over strong bonds in C<sub>3</sub>H<sub>8</sub>. C<sub>3</sub>H<sub>8</sub> conversion rates increase with residence time and NO, O<sub>2</sub>, and H<sub>2</sub>O pressures and exhibit supra-linear dependence on C<sub>3</sub>H<sub>8</sub> pressure with trends analogous to homogeneous systems involving H-abstraction by OH radicals but significantly different from V<sub>2</sub>O<sub>5</sub> catalysts that exhibit linear C<sub>3</sub>H<sub>8</sub> pressure dependence and weak sensitivity to the other parameters. Temperature dependencies of rate-constant-ratios representing activation energy differences between primary and secondary  $C_3H_8$  and allylic  $C_3H_6$  C-H bonds in  $NO_x$ -catalyzed routes are much weaker than  $V_2O_5$ , consistent with dampened bond-strength sensitivity that is also observed in density functional theory estimates of these differences for OH radicals. NO<sub>x</sub> mediation enables efficient alkane activation providing high productivity and yields at moderate temperatures, which is important for chemical transformations requiring rate-limiting C-H activation.

KEYWORDS: C-H activation, nitric oxide, OH radicals, strong abstractors, oxidative dehydrogenation, selective oxidation, H-atom addition energy

#### 1. INTRODUCTION

Selective formation of alkenes and oxygenates via alkane activation in exothermic oxidative routes remains challenging because products undergo more facile secondary C-H bond activation or C-O bond formation than reactants. 1,2 Systems reported to exhibit high propene (C<sub>3</sub>H<sub>6</sub>) yields in oxidative dehydrogenation (ODH) of propane (C<sub>3</sub>H<sub>8</sub>) on metal oxide catalysts and in gas-phase homogeneous reactions are summarized in Table S1 and Figure S1. Most oxide catalysts exhibit single-pass C<sub>3</sub>H<sub>6</sub> yields below 20% and approach with increasing temperature values attainable in gas-phase C<sub>3</sub>H<sub>8</sub>-O<sub>2</sub> reactions in empty reactors;<sup>3</sup> some alkali and halogen promoted oxides lead to 20-30% C<sub>3</sub>H<sub>6</sub> yields at high temperatures via routes that tend to involve both homogeneous and heterogeneous contributions.4 Improvements in C<sub>3</sub>H<sub>6</sub> selectivity with increasing temperatures in heterogeneous reactions are attributed to the lower activation energy for secondary reactions. These studies show significant differences in kinetic details between solid catalysts and homogeneous gas-phase reactions. The reactions on solid oxides are typically first- and zero-order in alkane and O<sub>2</sub> pressures, respectively, while rates on the latter systems tend to exhibit higher-order dependence on pressures of these reactants.<sup>5</sup>

Recent reports of high selectivity to C<sub>3</sub>H<sub>6</sub> and C<sub>2</sub>H<sub>4</sub> in C<sub>3</sub>H<sub>8</sub>-O<sub>2</sub> reactions on boron-based catalysts<sup>6-15</sup> have attracted significant interest in understanding the origins of the reactivity of these materials previously considered inert. The boron nitride systems were shown to require treatments that restore nitrogen content for sustained performance, suggesting that nitrogen atoms are important, 10 but reactions were also reported to proceed efficiently in other boron-based starting materials without nitrides. <sup>7,14</sup> In spite of the requirement of solid-boronbased surfaces, these systems seem to exhibit supra-linear reaction orders in C<sub>3</sub>H<sub>8</sub> and nonzero orders in O<sub>2</sub> pressures similar to homogeneous systems, pointing to some uniqueness in reaction steps involved.

Here, we report alternative selective dehydrogenation pathways involving homogeneous C<sub>3</sub>H<sub>8</sub>-O<sub>2</sub> reactions enhanced by

Received: September 9, 2019 Revised: October 3, 2019 Published: October 4, 2019



10324

addition of trace concentrations of NO and assess how mechanistic details and selectivity limitations for this system compare with solid catalysts. In these reactions, the NO and NO<sub>2</sub> (NO<sub>r</sub>) species undergo oxidation reduction catalytic cycles to release highly reactive OH radicals, which provide an important practical route to selective oxidative conversion of hydrocarbons at moderate temperatures. The effects of pressures of reactants and cofed H2O on measured alkane conversion rates and energies of reactive species and transition states from density functional theory (DFT) are used to infer mechanistic details of NO<sub>x</sub> catalysis, identify the types of radicals and reactive species involved, and determine conditions important for maximizing selectivity to desired products. The OH radicals generated in NO<sub>x</sub> catalytic cycles are strong abstractors of H-atoms in strong C-H bonds, and therefore, they activate C-H bonds via exothermic steps with early C-H activation transition states that cannot differentiate between strong and weak bonds in alkanes and product alkenes, respectively. Such dampening of bond-strength effects on activation rates and its relation to selectivity improvements in C<sub>3</sub>H<sub>8</sub> ODH are probed via temperature dependences of rate constant ratios relevant to selectivity and DFT calculations for C-H activation energy differences between C<sub>3</sub>H<sub>8</sub> and the C<sub>3</sub>H<sub>6</sub> product.

## 2. $C_3H_8$ ACTIVATION RATES AND SELECTIVITIES IN $C_3H_8-O_2-NO$ REACTIONS

Figure 1 shows the effect of NO pressure on C<sub>3</sub>H<sub>8</sub> conversion and product selectivity in empty flow reactors of two different

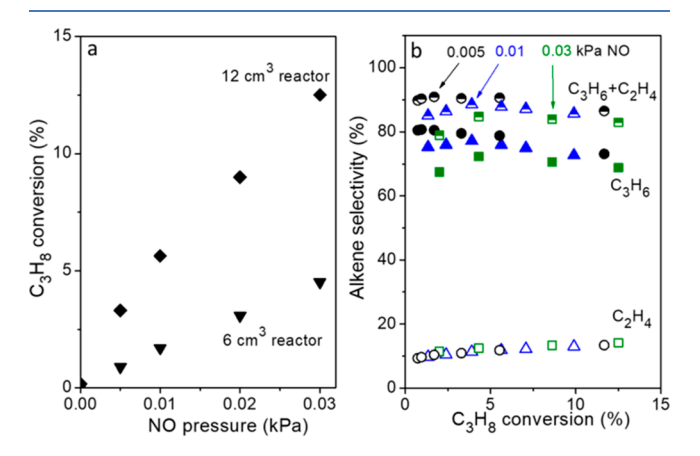


**Figure 1.** (a)  $C_3H_8$  conversion in 6 and 12 cm<sup>3</sup> reactors as a function of NO pressure at 30 cm<sup>3</sup> min<sup>-1</sup> flow rate, and (b) alkene selectivity as a function of  $C_3H_8$  conversion for different residence times in 12 cm<sup>3</sup> quartz reactor (773 K, 3 kPa  $C_3H_8$ , 10 kPa  $O_2$ , 0–0.03 kPa NO).

sizes (6 and 12 cm³ volumes; details in Figure S3). At the given reaction conditions (773 K, 3 kPa  $C_3H_8$ , 10 kPa  $O_2$ , 30 cm³ min⁻¹),  $C_3H_8$  exhibits conversions below 0.1% in the absence of NO, but the introduction of 0.005 kPa NO increases the conversion by factors of 35 and 20 for the 6 and 12 cm³ reactors, respectively. The incorporation of NO leads to additional  $C_3H_8$  reactions that are up to two or more orders of magnitude higher than the number of NO molecules added, depending on residence times and alkane pressures used, which suggests that NO acts as a catalyst instead of getting stoichiometrically consumed in the reaction. This catalytic role of  $NO_x$  in hydrocarbon conversion has been proposed and probed mechanistically in many previous studies.¹6−25 Such large

enhancements lead to homogeneous reactions rates comparable to those on solid catalysts, as shown in the Supporting Information via comparisons of productivity of NO<sub>x</sub>-mediated reactions with several previously reported catalytic reactions (Table S2), which may make it practical to run these reactions at large scales. The C<sub>3</sub>H<sub>8</sub> conversion increases with increasing NO pressure and is greater for the larger reactor, suggesting that reactions proceed in the gas-phase via homogeneous pathways enabled by NO or its oxidation products. The conversions increase more significantly than reactor volumes (Figure 1a) because rates are higher at longer residence times; such nonlinear residence time effects are further probed in section 4. C<sub>3</sub>H<sub>8</sub>-O<sub>2</sub> reactions at 0.005 kPa NO and conversions below 5% exhibit C<sub>3</sub>H<sub>6</sub> and C<sub>2</sub>H<sub>4</sub> selectivity near 80% and 10%, respectively (Figure 1b), total C1-C3 oxygenates selectivities near 7%, and total CO and CO<sub>2</sub> selectivity below 3% (detailed product selectivities in Figure S6a). The C<sub>3</sub>H<sub>6</sub> selectivity decreases weakly with conversion, consistent with higher yields than those typically attained on oxide catalysts, as also reported in the case of boron nitride catalysts. The formation of  $C_2H_4$  is consistent with C-C bond cleavage typically observed when homogeneous pathways mediate C<sub>3</sub>H<sub>8</sub> activation, which point to mechanistic similarities between NO-catalyzed reactions and the homogeneous reactions previously reported. 3,4,26 Higher NO feed concentrations enhance C<sub>3</sub>H<sub>8</sub> conversion rates more significantly but cause a slight decrease in C<sub>3</sub>H<sub>6</sub> selectivity at low conversions (Figure 1b), suggesting that an optimum low NO concentration maximizes the alkene selectivity at a given conversion.

Large enhancements in rates of alkane activation by NO<sub>r</sub> have been studied previously for the direct conversion of CH4 to oxygenate such as HCHO. 19,27 The NO<sub>x</sub>-catalyzed reactions led to greater HCHO selectivity than heterogeneous routes, but the yields remained well below 10% and significant side reactions that introduced nitrogen into hydrocarbons were observed due to large NO<sub>x</sub> feed concentrations up to 5 kPa. We show here that much smaller NO concentrations can be used to selectively convert C<sub>3</sub>H<sub>8</sub> to alkenes (Figure 1b; Section S4). Such small concentrations of NO are present as impurities in industrial exhaust gases  $^{28-30}$  that may  $\bar{b}e$  added to hydrocarbons and  $O_2$  to carry out the desired oxidative conversions. For example, power plant boilers and other sources such as industrial boilers, incinerators, and gas turbines operating at high temperatures produce  $NO_x$  by oxidizing  $N_2$  or nitrogen-containing fuels, leading to concentrations up to 300 and 1000 ppm at operating temperatures of 1350 K<sup>30</sup> and 1750 K,<sup>31</sup> respectively. Flue gases from these sources can be mixed with C<sub>3</sub>H<sub>8</sub>-O<sub>2</sub> mixtures for production of alkenes and other oxygenates using NO<sub>x</sub> at much lower temperatures and for potentially avoiding more expensive NO<sub>x</sub> treatments.

The mechanism of  $NO_x$ -catalyzed conversions of hydrocarbons such as  $CH_4$  involve the generation of OH radicals. These radicals have been detected by laser-induced fluorescence measurements for  $CH_4/O_2/NO_x$  reactions and their role as predominant abstractors of H-atoms from strong C-H bonds has been determined from kinetic simulations. The OH radicals generated from  $H_2O$  and  $O_2$  in alkali promoted oxides and molten salt catalysts at high temperatures have also been shown to activate hydrocarbons. Therefore, we probe the role of  $H_2O$  in further enhancing  $NO_x$ -mediated  $C_3H_8$  conversions by cofeeding  $H_2O$  to  $C_3H_8-O_2$  reactants with and without  $NO_x$  catalysts, as shown in Figure 2. When no  $H_2O$  is cofed (0 kPa  $H_2O$  in Figure 2a), the  $C_3H_8$  conversion is near

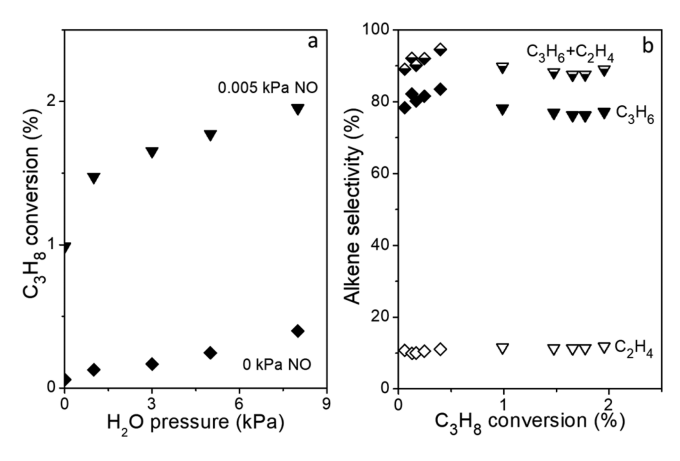


**Figure 2.** (a)  $C_3H_8$  conversion as a function of cofed  $H_2O$  pressure (at 30 cm<sup>3</sup> min<sup>-1</sup>), and (b) alkene selectivity as a function of  $C_3H_8$  conversion at different residence times (diamonds, 0 kPa NO; triangles, 0.005 kPa NO; 773 K, 3 kPa  $C_3H_8$ , 10 kPa  $O_2$ , 0–8 kPa  $H_2O$ , 6 cm<sup>3</sup> reactor).

1% for 0.005 kPa NO<sub>x</sub>, which is much higher than conversion without NO<sub>x</sub>. At this conversion, the average pressure of H<sub>2</sub>O produced from C<sub>3</sub>H<sub>8</sub>-O<sub>2</sub> reactions are near 0.01 kPa H<sub>2</sub>O<sub>3</sub> which is much less than the cofed water pressures. The addition of 1 kPa H<sub>2</sub>O for 0.005 kPa NO<sub>x</sub> increases the conversions to nearly 1.5%; for reactions without NO<sub>x</sub>, the conversion increase is much smaller. Further increase in cofed H<sub>2</sub>O pressure increases the C<sub>3</sub>H<sub>8</sub> conversion with slightly greater sensitivity for reactions with NO<sub>x</sub>. Thus, H<sub>2</sub>O enhances reaction rates more significantly when NO<sub>x</sub> is present, suggesting that it acts as a promoter or a cocatalyst for NO<sub>x</sub>-catalyzed OH radical generation. The alkene selectivities remain similar for reactions with and without NO, and exhibit weak sensitivity to conversion (Figure 2b), suggesting that similar reactive species can be responsible for alkane activations in both cases. These reactive species have been proposed and shown to be OH radicals in previous homogeneous reaction studies. 19,27,32

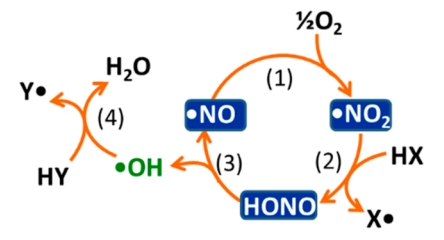
Next, we propose mechanistic details involving catalytic reactions of  $NO_x$  and  $H_2O$  that lead to rate enhancements in gasphase  $C_3H_8-O_2$  reactions shown in Figures 1 and 2. We probe the feasibility of these reactions using DFT-derived H-abstraction strengths of gaseous reactive species, C–H bond strengths for different types of bonds in C3 hydrocarbons and organic radicals, C–H bond activation energies and experimental activation energies available in the literature, and electronic energies and Gibbs free energies for reactions involved in catalytic steps. These assessments are used to establish the nature of active species relevant for the selective gas-phase oxidative dehydrogenations.

# 3. OH RADICAL GENERATION VIA $NO_\chi$ CATALYSIS AND MECHANISTIC CONNECTIONS OF RATE AND SELECTIVITY ENHANCEMENTS TO STRENGTHS OF H-ABSTRACTORS AND C-H BONDS

# **3.1.** H-Abstractors Generated in $NO_x$ Catalytic Cycles. Previous kinetic simulations for $CH_4-O_2-NO_x$ reactions suggest that $NO_2$ formed via NO oxidation facilitates pathways that generate OH radicals, which are strong abstractors of Hatoms in $CH_4$ , and reform NO to complete $NO_x$ catalytic cycles, <sup>16</sup> without NO getting stoichiometrically consumed in the process. <sup>19,27</sup> Dehydrogenations of saturated hydrocarbons and oxygenates occur via homolytic C-H activation steps at H-

abstracting oxidants,  $^{2,35}$  indicating that mechanisms similar to CH<sub>4</sub> activation are also relevant to C<sub>3</sub>H<sub>8</sub> dehydrogenation. Scheme 1 shows such catalytic cycles involving interactions of

Scheme 1. NO<sub>x</sub> Catalytic Cycles Generating OH Radicals<sup>a</sup>



<sup>a</sup>HX and HY represent organic molecules activated by C–H activation.

NO<sub>x</sub> with oxidant O<sub>2</sub> and reductant hydrocarbons. The oxidation of NO to ●NO<sub>2</sub> (step 1, Scheme 1) can occur via well-established kinetics with rates proportional to O<sub>2</sub> pressure and the square of NO pressure, and with slightly negative activation energy that indicates facile nature of this step. 36 This reaction is mediated by a kinetically relevant step involving a trimolecular transition state.  $^{37-40}$  The NO<sub>2</sub> molecule abstracts an H-atom from a saturated organic molecule (HX; e.g., C<sub>3</sub>H<sub>8</sub>) to form HONO and an organic radical species (X•, step 2, Scheme 1). The HONO species dissociates to form OH radical and NO molecule (step 3). The OH radicals generated in this cycle also abstract H-atoms from organic molecules (HY) to form organic radical species (Y•) and H<sub>2</sub>O (step 4). These cycles are analogous to Mars van Krevelen (MvK) redox cycles ubiquitous in selective oxidation of organic molecules on oxides where facile O<sub>2</sub> activation forms an oxidized form of the catalyst, which is reduced via kinetically relevant C-H activation steps to form surface OH species that dehydroxylate to form H<sub>2</sub>O and Ovacancies. <sup>41–44</sup> The redox cycles for NO<sub>x</sub>, however, can generate highly energetic gaseous OH species instead of surface oxygen species.

The OH radicals exhibit a strong tendency to abstract Hatoms from strong C-H bonds, as proposed in many previous studies. 4,16,17,19,21,26,34,45 Their formation according to Scheme 1, however, requires a sacrificial H-abstraction by NO2 to generate HONO precursors. The HX and HY molecules in Scheme 1 represent different or the same organic molecules depending on the types of species present during reactions and the reactivity preferences dictated by the strengths of the abstractors and C-H bonds. HX represents a sacrificial species with weak C-H bonds that can activate C-H bonds by NO<sub>2</sub> as an abstractor for facile HONO formation. Previous kinetic simulations for CH<sub>4</sub>-O<sub>2</sub>-NO<sub>x</sub> reactions found that CH<sub>4</sub> itself acts as the sacrificial species near zero conversion during the induction period when weaker C-H bonds are not present, but at finite conversions oxygenate species such as HCHO molecules and HCO radicals with very weak C-H bonds can be the sacrificial H-donors. 18,19,22-24,27 The organic radicals (X• and Y.) further react with oxidants to form unsaturated or oxidized organic molecules (e.g., C<sub>3</sub>H<sub>6</sub>, HCHO). Species with weak C-H bonds may activate on weaker abstractors, leading to several possibilities including C-H bond activation in organic species occurring directly at HONO, NO, or O2 to form H2O +NO, HNO, and •OOH species, respectively. These plausible steps for the activation of C<sub>3</sub>H<sub>8</sub> and C<sub>3</sub>H<sub>7</sub> radicals by different oxidants are shown in Scheme 2.

Scheme 2. C-H Activations in C<sub>3</sub>H<sub>8</sub> and C<sub>3</sub>H<sub>7</sub> Radical by Different Oxidant Species Involved in NO<sub>x</sub> Catalytic Cycles

$C_3H_8 + \bullet NO \longrightarrow$	$\bullet C_3H_7 + HNO$	(1)
$C_3H_8 + O_2 \longrightarrow$	$\bullet C_3H_7 + \bullet OOH$	(2)
$C_3H_8$ + HONO $\longrightarrow$	$\bullet C_3H_7 + H_2O + \bullet NO$	(3)
$C_3H_8 + \bullet NO_2 \longrightarrow$	${ullet} C_3H_7 + HONO$	(4)
C <sub>3</sub> H <sub>8</sub> + •OOH	$\bullet C_3H_7 + H_2O_2$	(5)
C <sub>3</sub> H <sub>8</sub> + •OH	$\bullet$ C <sub>3</sub> H <sub>7</sub> + H <sub>2</sub> O	(6)
•C <sub>3</sub> H <sub>7</sub> + •NO	C <sub>3</sub> H <sub>6</sub> + HNO	(1')
$\bullet C_3H_7 + \bullet NO \longrightarrow \\ \bullet C_3H_7 + O_2 \longrightarrow $	$C_3H_6 + HNO$ $C_3H_6 + \bullet OOH$	(1') (2')
$\bullet C_3H_7 + O_2 \longrightarrow$	$C_3H_6 + \bullet OOH$	(2')
	$C_3H_6 + \bullet OOH$ $C_3H_6 + H_2O + \bullet NO$	(2') (3')
$\begin{array}{cccccccccccccccccccccccccccccccccccc$	$C_3H_6 + \bullet OOH$ $C_3H_6 + H_2O + \bullet NO$ $C_3H_6 + HONO$	(2') (3') (4')

These possibilities lead to complex reaction networks in which only some of the many steps contribute to most of the observed rates and to selectivity limitations. 18,19,22-24,27 Kinetic analyses for such systems require knowledge of rate constants for all possible steps. Many of these constants for CH<sub>4</sub> oxidation are available from experiments but require further modifications for kinetic simulations. Analogous analyses for C<sub>3</sub>H<sub>8</sub> oxidation are more complex than CH<sub>4</sub> and involve greater uncertainty in values of rate constants due to the significantly greater number and structural complexity of possible organic species involved as minor products. Yet, trends in reactivity of the catalytic species present in reaction can be determined using thermodynamic properties reflected in bond strengths in reactants and abstractors derived from DFT calculations. Analyses based on these reactivity trends are used here to derive mechanistic insights and assess relevance of reactive species to rates and selectivity, instead of numerical data based on tabulated rate constants and activation energies. We probe which of the possible steps may prevail at reaction conditions by examining the strengths of C-H bonds and abstractors involved in the steps shown in Scheme 2.

**3.2. Strengths H-Abstractors and C–H Bonds.** The H-abstraction strengths of the various molecular species involved in catalytic cycles of  $NO_x$  (Schemes 1 and 2) and of lattice O-atoms of the  $V_2O_5(001)$  surface used as a representative solid oxide catalyst are given by the DFT-derived values of H-atom addition energy (HAE) shown in Table 1. The DFT calculations

Table 1. DFT (PBE-D3BJ)-Derived Electronic Energies for H-Atom Addition to H-Abstractors

H-abstractor	Structures	HAE (kJ mol <sup>-1</sup> )
• <u>N</u> O	<b>⊕</b>	-179
$\underline{O}_2$	<b>9−9</b>	-221
H <u>O</u> NO	J	-256
$\bullet N\underline{O}_2$	•••	-319
• <u>O</u> OH	6-0	-365
• <u>O</u> H	<b>○6</b>	-520
V= <u>O*</u>		-292

were performed using PBE-D3BJ DFT functionals  $^{46}$  within the Vienna Ab-Initio Simulation Package. Gas molecules were simulated in a 20 Å cubic box with dipole corrections, and  $V_2O_5(001)$  surface were simulated using two layers of orthorhombic oxide repeating periodically in lateral directions and vacuum separation in (001) direction. Additional details of computational methods and catalyst models are provided in Section S2.4. More negative HAE values represent stronger Habstractors that tend to be more reactive for C–H bond activation.

The HAE values range from  $-179 \text{ kJ mol}^{-1}$  to  $-520 \text{ kJ mol}^{-1}$  for the weakest (NO) to the strongest (OH) abstractor in Schemes 1 and 2. The HAE value for the O-atom in terminal V=O\* species in V<sub>2</sub>O<sub>5</sub>, the most reactive site on this oxide, is  $-292 \text{ kJ mol}^{-1}$ . Weak H-abstractors NO, O<sub>2</sub>, and HONO exhibit HAE values less negative than the lattice O-atoms of V<sub>2</sub>O<sub>5</sub>. As a result, these species are unlikely to directly abstract strong C-H bonds in alkanes. NO<sub>2</sub> and OOH radical species are stronger abstractors than V<sub>2</sub>O<sub>5</sub>, while OH radicals are much stronger than even OOH (Table 1). These values are consistent with the catalytic cycle proposed in Scheme 1, where C-H bonds are abstracted from NO<sub>2</sub> and OH radicals instead of the weak abstractors such as NO. The strong H-abstraction propensity of OH radicals leads to high reactivity of this abstractor for strong C-H bonds.

Table 2 shows the strength of C-H bonds in  $C_3H_8$ , in dehydrogenation product  $C_3H_6$ , and in radicals formed by first

Table 2. C–H Bond Dissociation Enthalpy ( $\Delta H_{\rm C-H}^0$  at 298.15 K) and Electronic Energy ( $\Delta E_{\rm C-H}^0$ ) in C3 Hydrocarbons and Radicals

		$\Delta H_{C-H}^{0}$ (kJ mol <sup>-1</sup> )		$\Delta E_{\mathrm{C-H}_{\perp}}^{0}$
molecule	C– <u>H</u> bond	measured <sup>47</sup>	DFT-derived (PBE-D3BJ)	(kJ mol <sup>-1</sup> ) (PBE-D3BJ)
$C_3H_8$	$CH_3C\underline{H}_2CH_3$	411	391	421
	$C\underline{\mathbf{H}}_3CH_2C\underline{\mathbf{H}}_3$	422	408	438
$C_3H_6$	$CH_2 = CHC\underline{H}_3$	363	345	371
	$C\underline{\mathbf{H}}_2$ = $CHCH_3$		452	478
	$CH_2 = C\underline{H}CH_3$		427	454
$\bullet C_3H_7$	C <u>H</u> ₃•CHC <u>H</u> ₃		159	174
	$\bullet CH_2C\underline{H}_2CH_3$		142	157
$\bullet C_3H_5$	$CH_2 = C\underline{H} \bullet CH_2$		235	256

C–H activation in these molecules, as reflected in their experimental and PBE-D3BJ-derived bond dissociation enthalpies and electronic energies (BDE). Larger BDE values represent stronger C–H bonds that exhibit higher C–H activation energy for a given H-abstractor. The DFT-derived enthalpies are slightly lower than experimental values but exhibit similar differences among different types of C–H bonds as observed in measurements. 35,47

The electronic C–H BDE values for different types of C–H bonds in  $C_3H_8$  and  $C_3H_6$  range from +371 kJ mol<sup>-1</sup> to +478 kJ mol<sup>-1</sup>. The BDE value is higher for the primary C–H bond in  $C_3H_8$  (438 kJ mol<sup>-1</sup>) than the secondary C–H bond (421 kJ mol<sup>-1</sup>, Table 2), suggesting that the secondary bonds are more reactive for homolytic C–H activations. The vinylic C–H bonds of the  $C_3H_6$  are much stronger than both primary and secondary bonds in  $C_3H_8$  (478 and 454 kJ mol<sup>-1</sup>, Table 2), suggesting that these bonds are much less reactive. In contrast, the allylic C–H bonds in  $C_3H_6$  are weaker than the bonds in  $C_3H_8$  (371 kJ mol<sup>-1</sup>, Table 2), which indicates that the  $C_3H_6$  molecule can

undergo facile C–H activations at the allylic position and is more reactive for C–H activations than the reactants. Such allylic C–H activations are often rate-limiting steps in oxidation of  $\rm C_3H_6$ .  $^{48-51}$   $\rm C_3H_6$  is the desired product in  $\rm C_3H_8$  oxidative dehydrogenation, and therefore, these facile C–H activations represent the most significant limitations to the selectivity to this product on typical transition metal oxide catalysts such as  $\rm V_2O_5$  because they lead to more facile activation of weaker C–H bonds.

The C–H BDE values for propyl radical species formed by first C–H activation in  $C_3H_8$  are much lower than all bonds in  $C_3H_8$  and  $C_3H_6$  (157 and 174 kJ mol<sup>-1</sup> for primary and secondary radicals, respectively; Table 2), which is indicative of the much more reactive nature of these radicals. The C–H BDE for the allyl radial formed from  $C_3H_6$  is higher than propyl radicals, but it remains much lower than  $C_3H_8$  and  $C_3H_6$  molecules suggesting their reactive nature.

Next, we probe the effect of the BDE and the HAE values on DFT-derived C-H activation energies given by differences in electronic energy between the C-H activation transition state and the isolated abstractor and hydrocarbon. These trends are used to determine preferences for the abstractors for the activation of the different organic molecules and radicals in Table 2 and the most likely abstractors involved in  $C_3H_8$  activation in the  $NO_x$ -mediated catalytic cycles shown in Scheme 1.

**3.3. Effects of Abstractor Strengths and C–H Bond Strengths on C–H Activation Energies.** The C–H activation energies derived from PBE-D3BJ calculations for a secondary C–H bond in  $C_3H_8$  ( $CH_3C\underline{H}_2CH_3$ , Table 2) to form a secondary  $C_3H_7$  radical, for a C–H bond in the secondary  $C_3H_7$  radical ( $C\underline{H}_3 \bullet CHC\underline{H}_3$ ) to form the desired  $C_3H_6$  product, and for an allylic C–H bond in  $C_3H_6$  ( $CH_2 = CHC\underline{H}_3$ ), as a function of HAE of the H-abstractors in Table 1 are shown in Figure 3. These C–H activations shown here represent the sequence of steps required to form the desired  $C_3H_6$  product and its secondary reactions ( $C_3H_8 \rightarrow \bullet C_3H_7 \rightarrow C_3H_6 \rightarrow \bullet C_3H_5$ ); thus, activation energy differences among these steps are relevant to  $C_3H_6$  selectivity.

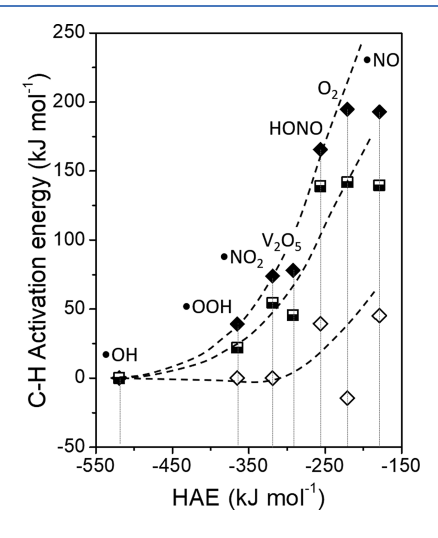


**Figure 3.** Activation energies derived from PBE-D3BJ calculations for  $C-\underline{H}$  bonds in  $CH_3C\underline{H}_2CH_3$  ( $\spadesuit$ ),  $C\underline{H}_3$ • $CHC\underline{H}_3$  ( $\diamondsuit$ ) and  $CH_2$ = $CHC\underline{H}_3$  (half-filled squares) as a function of H-atom addition energies for abstractors shown in Table 1. Dashed lines show trends.

The C-H activation energies for a secondary C-H bond in C<sub>3</sub>H<sub>8</sub> are lower for stronger H-abstractors with more negative HAE values (CH<sub>3</sub>CH<sub>2</sub>CH<sub>3</sub>, Figure 3). This C-H bond is weaker and more reactive among the two types of C-H bonds in C<sub>3</sub>H<sub>8</sub> (Table 2). The activation energy is greater than 150 kJ mol<sup>-1</sup> for weak abstractors NO, O<sub>2</sub>, and HONO, near 75 kJ mol<sup>-1</sup> for NO<sub>2</sub> and V<sub>2</sub>O<sub>5</sub> abstractors of intermediate strength, and 39 kJ mol<sup>-1</sup> for the OOH radical. The OH radicals are much stronger H-abstractors than all other abstractors. The energy of the system decreases monotonically as the C<sub>3</sub>H<sub>8</sub> molecule approaches this abstractor and does not exhibit a local maximum indicative of a transition state (nudged elastic band calculation shown in Figure S20), which leads to an activation energy of zero. These trends in C<sub>3</sub>H<sub>8</sub> activation energy are consistent with experimental values reported in the literature for the different oxidants, which are shown in Table S4. The measured activation energies in literature are 200, 95, and 58 kJ  $\mathrm{mol}^{-1}$  for  $\mathrm{O}_2$ ,  $\mathrm{NO}_2$ , and the OOH radical and nearly zero for the OH radical.<sup>52-</sup> These predicted and measured activation energies suggest that the activation rates for OH radials are much higher than the other abstractors. Estimates form Arrhenius expression suggests that C<sub>3</sub>H<sub>8</sub> activation rates at 773 K for OH radical are larger than OOH radical by 3 orders of magnitude for the DFT-derived activation energy (+39 kJ mol<sup>-1</sup> for OOH, Figure 3) and by 4 orders of magnitude to measured values in the literature (+58 kJ mol<sup>-1</sup> for OOH<sup>54</sup>); other abstractors are much less reactive than both OH and OOH radicals. Thus, C<sub>3</sub>H<sub>8</sub> molecules will be activated preferentially by OH radicals even if the concentration of these radicals were much smaller than the concentrations of other abstractors. These estimates are consistent with the predominant role of OH radicals in homogeneous oxidations catalyzed by  $NO_x$  as well as alkali promoted and molten salt oxides.  $^{4,16-21,34}$ 

The C-H bond in the C<sub>3</sub>H<sub>7</sub> radical is much weaker than C<sub>3</sub>H<sub>8</sub>, leading to much lower activation energy for a given abstractor (CH<sub>3</sub>•CHCH<sub>3</sub>, Figure 3). The C−H activation energy for this radical is 45 and 40 kJ mol<sup>-1</sup>, for weak abstractors NO and HONO, respectively. For NO2 and OOH and OH radicals, the energies decrease monotonically as the  $C_3H_7$  radical approaches the abstractors, leading to zero activation energies.  $O_2$  forms a stable physiosorbed complex with the  $C_3H_7$  radical which undergoes C-H activation via a transition state with -14kJ mol<sup>-1</sup> activation energy relative to the isolated precursors. This negative activation energy is consistent with the experimental value of -9 kJ mol<sup>-1</sup> reported in the literature<sup>56</sup> (Table S4). Thus, in contrast to the  $C_3H_8$  molecule, the  $C_3H_7$ radical does not exhibit a strong preference for OH radicals as abstractors. The activation energy is near zero for several abstractors and it can be activated on several abstractor species, depending on the abundance of these species. The C<sub>3</sub>H<sub>7</sub> radical can also act as a sacrificial H-atom donor required to form HONO (Scheme 1). O<sub>2</sub> exhibits slightly negative activation energies and is fed at much higher concentrations than NO in the measurements (typical conditions: 3, 10, and 0.005 kPa  $C_3H_8$ ,  $O_2$ , and NO, respectively); thus,  $O_2$  is likely to activate most of the C<sub>3</sub>H<sub>7</sub> radicals.

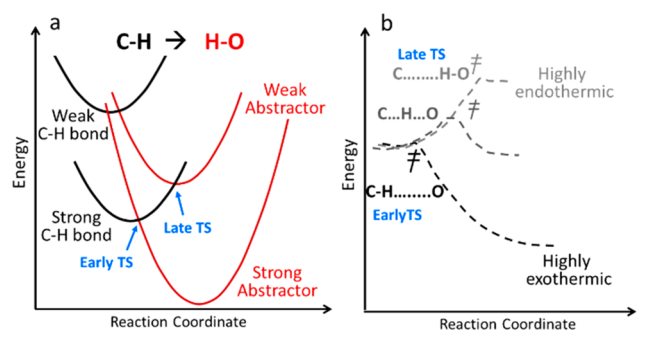
The C-H activation energies as a function of HAE were also calculated for a primary C-H bond in  $C_3H_8$  ( $C\underline{H}_3CH_2C\underline{H}_3$ , Table 2), and subsequent C-H activation in the primary radical to form  $C_3H_6$  are shown in Figure S14 and Table S6. These activation energies exhibit similar overall trends as that shown for the secondary C-H bond activation and the subsequent alkene formation (Figure 3). The activation energies for

 $C\underline{H}_3CH_2C\underline{H}_3$  are zero for OH radicals and 12-17 kJ mol<sup>-1</sup> higher than  $CH_3C\underline{H}_2CH_3$  for other abstractors, consistent with the less reactive nature of stronger primary C–H bonds. OH radicals, however, suppress these bond strength differences, leading to no activation energy difference between primary and secondary C–H bonds. The activation energies for both types of  $C_3H_7$  radicals are similar within 6 kJ mol<sup>-1</sup> (Figure 3, Figure S14, and Table S7).

Figure 3 also shows the activation energies for the allylic C-H bond in  $C_3H_6$ . This C-H bond is weaker than the bonds in  $C_3H_8$  by about 50 kJ mol<sup>-1</sup> but nearly 200 kJ mol<sup>-1</sup> stronger than the bonds in  $C_3H_7$  radicals (Table 2). As a result, the activation energies for  $C_3H_6$  are intermediate between the two species. The lower activation energies of  $C_3H_6$  than  $C_3H_8$  is consistent with low selectivity to the desired  $C_3H_6$  product observed on most oxide catalysts. The difference between the two activation energies diminishes as the abstractors become stronger and nearly zero for OH radicals, suggesting that stronger abstractors are more selective to  $C_3H_6$ .

The decrease in activation energies with increasing abstractor strength exhibits a curved trend with a smaller local slope for stronger abstractors (Figure 3), consistent with deviations from linear Brønsted–Evans–Polanyi (BEP) relations that have been observed for C–H and O<sub>2</sub> activations and C–O bond formation reactions on oxides. So,59–61 Such trends can be described by crossing-potential models that represent C–H activation transition state structures and their energies via the intersection point between harmonic potentials for C–H bond cleavage and O–H bond formation, as shown in Scheme 3.

## Scheme 3. Effect of C—H Bond Strength and H-Abstractor Strength on C—H Bond Activation<sup>a</sup>



a(a) Crossing of harmonic potentials for C-H cleavage and O-H formation, and (b) changes in lateness of transition sate (TS) with reaction energies.

The stretching of a C-H or an O-H bond beyond its equilibrium length increases the potential energy of the species, which is represented here by parabolic shape of the harmonic potential energy surface for these bonds (Scheme 3a). A lower vertical position of the minimum energy point of a parabola represents stronger bond strength. C-H activation requires breaking of a C-H bond and formation of an O-H bond, which can be represented by overlapping the potentials (parabolas) for a reactant C-H bond and a product O-H bond. The *x*-axis here represents the position of H-atom moving away for the C-atom and toward the O-atom. The intersection point of the two potentials represents the C-H activation transition state.

For a given C—H bond, the minimum energy point of the OH potential shifts to lower energy while keeping the same distance with the C—H bond minimum position along the *x*-direction as

the H-abstractor becomes stronger (stronger O–H bond) and the C–H activation step becomes more exothermic. As a result, the intersection-point appears at lower energies (*y*-axis) and at earlier points along the C–H stretching coordinate (*x*-axis). When the abstractors are very strong, the intersection occurs near the flat part of the C–H parabola near the equilibrium C–H bond position where the energy of the intersection point decreases weakly with lowering of the O–H parabola (Scheme 3a). These intersection points represent early transition states with barely stretched C–H bonds and activation energies near zero.

The crossing potential models accurately capture the general shape of the activation energy versus HAE trends in Figure 3. Some deviations from the trendlines appear because activation energies depend not only on bond-making and -breaking shown by crossing potentials but also on additional attractive radicalradical or dispersive van der Waals interactions between reacting species in the reactant and the product state, as shown recently.<sup>35</sup> The functional form of the dependence of activation energies on the reaction energies derived from such crossing potential models are analogous to the activation energy term in Marcus theory, 62 which accounts for the curvatures neglected in linear BEP relations.<sup>35</sup> Predictions from such models are also consistent with Hammond's postulate that more exothermic reactions occur via earlier transition states that are more reactant-like (Scheme 3b).<sup>63</sup> The small C-H bond elongation at early transition states, in turn, leads to activation energies insensitive to bond strengths.

For the C-H activation steps shown in Scheme 2 and the corresponding activation energies in Figure 3, the final state reaction energy is given by the summation of the C-H BDE in Table 2 and HAE in Table 1. The C-H BDE in  $C_3H_8$  and  $C_3H_6$ are larger than negative of the HAE of all abstractors except the OH radical. As a result, these reactions are endothermic for these weaker abstractors and highly exothermic for the OH radicals. As the reactions become less endothermic, the transition states appear earlier along the reaction coordinate and become less sensitive to bond strength. The DFT-derived bond-lengths of the transition states are shown in the Supporting Information, and they indeed exhibit shorter C-H and longer H-O bonds for more exothermic reactions (Figure S15). For OH radicals, the reaction is very exothermic, and the transition states are very early, leading to nearly complete insensitivity to bond strength and suppression of high reactivity for the weaker bonds. For weak C-H bonds in C<sub>3</sub>H<sub>7</sub> radicals, the reaction is exothermic and is mediated by early transition states for both strong and weak abstractors which leads several abstractors with near-zero activation energies (Figure 3). Thus, both calculated activation energies and fundamental conceptual assessments of the bond activation process point to the importance of OH radicals in selectively activating strong C–H bonds.

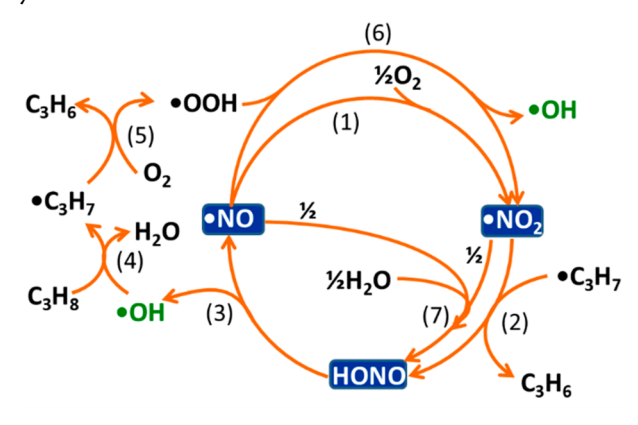
These analyses establish that (i) OH radicals can be generated from redox catalytic routes consisting of  $NO_x$  reduction oxidation steps reported in many past studies on  $NO_x$ -mediated hydrocarbon oxidations, (ii) OH radicals are very strong H-abstractors that activate strong C-H bonds in  $C_3H_8$  at rates several orders of magnitude higher than any other reactive species, which makes them the predominant  $C_3H_8$  activating species even when they are present at lower concentrations than other species, (iii) weak C-H bonds in  $C_3H_7$  radicals do not require strong H-abstractors and can be activated by  $NO_2$  and  $O_2$ , with  $O_2$  being more abundant, and (iv) OH radicals can

improve selectivity by dampening the preference exhibited by all other abstractors for activating  $C_3H_6$  over  $C_3H_8$ .

Next, we combine these insights with additional steps for consumption of OOH radicals and the role of  $H_2O$  in OH radical generation and use DFT calculations to assess energies of steps in a proposed reaction network for  $C_3H_8$  activation in  $NO_x$ -mediated routes.

3.4. Role of H<sub>2</sub>O and Alternative OH Radical Generation Paths. Scheme 4 shows more complete steps

Scheme 4. Primary  $C_3H_8$  Activation Routes in  $NO_x$  Catalytic Cycles



involved in NO<sub>x</sub>-mediated catalytic mechanism for OH radical generation and C<sub>3</sub>H<sub>8</sub> activation. Electronic energies, enthalpies, and Gibbs free energies derived from DFT calculations for the steps in this mechanism are shown in Table 3. NO<sub>2</sub> formation via NO-O2 reaction is highly exothermic, but its stoichiometry leads to fewer products than reactants, which results in entropy loss and slightly positive Gibbs free energies (22 kJ mol<sup>-1</sup>, step 1, Table 3;  $\Delta G = \Delta H - T\Delta S$ ). The mildly endoergic nature of this step (i.e., slightly positive  $\Delta G$ ) suggests that it will form a small but significant concentration of NO2 to reach equilibrium. Higher O<sub>2</sub> concentrations push this equilibrium toward the NO<sub>2</sub> product. C<sub>3</sub>H<sub>7</sub> radicals donate a H-atom to NO<sub>2</sub> to form HONO and  $C_3H_6$  (step 2 in Scheme 4) because this step was found to be facile based on calculated C-H activation energies in Figure 3; this step is also highly exothermic and exoergic. The OH radical formation by HONO dissociation (step 3) is highly endothermic but only mildly endoergic due to entropy gain from the formation of two molecules from one ( $\Delta G = +12 \text{ kJ}$  $\text{mol}^{-1}$ , step 3, Table 3). The OH radical activates  $C_3H_8$  to form

the  $C_3H_7$  radical and  $H_2O$ , in highly facile exothermic and exoergic steps (step 4). The  $C_3H_7$  radical activates an  $O_2$  molecule to form a OOH radical (step 5), which is also facile. This OOH radical can react with NO to form  $NO_2$  and OH radical (step 6), which is much more facile than NO oxidation by  $O_2$  (step 1). Previous kinetic simulations have shown that step 6 can lead to rapid NO oxidation, forming  $NO_2$  in greater concentrations than the equilibrium value for step  $1.^{19}$  These details show that  $NO_x$  can catalyze OH radical generation and  $C_3H_8$  activation in a series of facile steps.

H<sub>2</sub>O enhances C<sub>3</sub>H<sub>8</sub> conversion in C<sub>3</sub>H<sub>8</sub>-O<sub>2</sub> reaction and does so to a much greater extent for NOx-catalyzed reactions than reactions without  $NO_x$  (Figure 2). These enhancements are consistent with the role of water in generating OH radicals in molten salt catalysts and the facile reactions of NO<sub>x</sub> to form HONO even at room temperature.<sup>64</sup> The HONO formation via the NO-NO2-H2O reaction is exothermic and moderately endoergic at the reaction temperature (step 7, Scheme 4 and Table 3,  $\Delta H = -35 \text{ kJ mol}^{-1}$ ,  $\Delta G = +53 \text{ kJ mol}^{-1}$ , 773 K), suggesting formation of small but significant concentrations of HONO using high H<sub>2</sub>O pressures to push equilibrium toward products. DFT calculations for this reaction are shown in Figure S22. These calculations show that NO, NO2, and H2O form a trimolecular complex and form HONO via a transition state with negative electronic activation relative to isolated molecules. Lower temperatures lead to a less exoergic nature of this step due to lesser contribution of entropy loss to free energy. The HONO molecules then dissociate to form OH radicals (step 3). Another step involving HONO and HONO2 from NO2 and H2O is shown in Table 3 (step 8). This step is also mildly endoergic and suggests another route to a species that dissociates to form OH radicals. This reaction was also found to be facile in experiments reported in the literature. 65,66 Thus, several steps involved in catalytic redox cycles of NO<sub>x</sub> generate OH radicals (Scheme 4). These radicals can also be quenched to form O<sub>2</sub> and H<sub>2</sub>O (step 9, Table 3), which leads to low concentration of these radicals. This highly potent nature of these radicals leads to enhanced C<sub>3</sub>H<sub>8</sub> activations even at these low concentrations. Formation of such abstractors without NO<sub>x</sub> would require direct initial alkane activation on O2, which has very high activation energies (Figure 3, Scheme 2). NO<sub>x</sub> facilitates OH radical generation at moderate temperature by forming stable NOx-derived species that enhance OH radical formation at moderate temperature. At finite C<sub>3</sub>H<sub>8</sub> conversions organic species other than C<sub>3</sub>H<sub>8</sub> exist in the reaction mixture, including alkenes and oxygenate formed as minor products. Plausible steps for formation of these products

Table 3. Electronic Energies, Enthalpies, and Gibbs Free Energies at 773 K, Derived from PBE-D3BJ Level of Theory, a for Reaction Steps in Scheme 4

no.	reaction	$\Delta E \text{ (kJ mol}^{-1}\text{)}$	$\Delta H$ (kJ mol <sup>-1</sup> )	$\Delta G$ (kJ mol <sup>-1</sup> )
1	$\bullet$ NO + $^{1}/_{2}$ O <sub>2</sub> $\rightarrow$ $\bullet$ NO <sub>2</sub>	-111	-121	22
2	$\bullet$ NO <sub>2</sub> + $i$ - $\bullet$ C <sub>3</sub> H <sub>7</sub> $\rightarrow$ C <sub>3</sub> H <sub>6</sub> + HONO	-144	-140	-99
3	$HONO \rightarrow \bullet OH + \bullet NO$	267	271	12
4	$C_3H_8 + \bullet OH \rightarrow i - \bullet C_3H_7 + H_2O$	-99	-106	-121
5	$i - \bullet C_3H_7 + O_2 \rightarrow C_3H_6 + \bullet OOH$	-46	-45	-58
6	$\bullet$ NO + $\bullet$ OOH $\rightarrow$ $\bullet$ NO <sub>2</sub> + $\bullet$ OH	-52	-66	14
7	$^{1}/_{2} \bullet NO + ^{1}/_{2} \bullet NO_{2} + ^{1}/_{2}H_{2}O \rightarrow HONO$	-33	-35	53
8	$\bullet NO_2 + {}^{1}/{}_{2}H_2O \rightarrow {}^{1}/{}_{2}HNO_2 + {}^{1}/{}_{2}HNO_3$	-21	-13	39
9	$\bullet$ OOH + $\bullet$ OH $\rightarrow$ H <sub>2</sub> O + O <sub>2</sub>	-299	-297	-159

<sup>&</sup>quot;Pressures of  $C_3H_8$ ,  $O_2$ ,  $H_2O$ ,  $C_3H_6$ ,  $\bullet$ NO, and  $\bullet$ NO<sub>2</sub>: 3, 10, 10, 1, 0.01, and 0.01 kPa, respectively, based on typical feed and moderate conversion;  $\bullet$ OOH, HONO,  $i\bullet C_3H_7$ : 0.001 kPa;  $\bullet$ OH: 0.0001 kPa.

and some activation energies from experimental measurements of these steps reported in the literature are shown in Schemes S1,2 and Table S5. These products also contain weak C–H bonds and can promote H-abstraction by NO<sub>2</sub> to further enhance concentrations of HONO and OH radicals, as shown via experiments and kinetic simulations for HCHO formations in  $\text{CH}_4$ – $\text{O}_2$ – $\text{NO}_x$  reactions.  $^{18,19,22-24,27}$ 

Next, we compare reaction rates and selectivity in this  $NO_x$ -mediated OH radical based reactions with  $V_2O_5$  catalysts to assess the effect of abstractor strength on rates and selectivity.

# 4. DIFFERENCES IN RATES AND SELECTIVITY BETWEEN $NO_{\chi}$ -MEDIATED PATHWAYS AND $V_2O_5$ CATALYSTS

C<sub>3</sub>H<sub>8</sub> activation on vanadium-based oxide catalysts occurs via MvK redox cycles, where lattice oxygen species shown in Table 2 (V=O\* species) act as predominant H-abstractors. C-H activations at these sites lead to reduced centers existing as OH pairs or as O-vacancies formed by dihydroxylations at OH pairs. These reduced centers are reoxidized by rapid O<sub>2</sub> activations to restore the V=O\* sites. The rapid nature of the reoxidation steps leads to most of the catalyst existing as V=O\* and nearly fixed number of these abstractors at different reaction conditions. 1,42,67 In contrast, the NO<sub>x</sub>-mediated cycles lead to OH radicals as predominant abstractors of strong C-H bonds in C<sub>3</sub>H<sub>8</sub>. The concentration of these abstractors varies with reaction conditions due to changes in concentrations of sacrificial H-atom donors to NO<sub>2</sub> (step 2 in Schemes 1 and 4) and presence of H<sub>2</sub>O (step 7 in Scheme 4). These differences influence how change in C<sub>3</sub>H<sub>8</sub> conversion via changing residence time affects reaction rates in the two types of reactions. Figure 4 shows C<sub>3</sub>H<sub>8</sub> activation rates and product

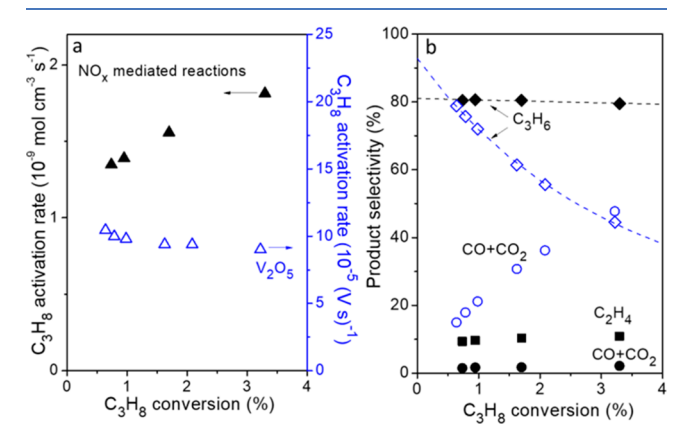


**Figure 4.** (a)  $C_3H_8$  activation rates and (b) selectivity to alkenes, CO, and CO<sub>2</sub> as a function of  $C_3H_8$  conversion, in 12 cm<sup>3</sup> empty reactor with 0.005 kPa NO (closed symbols) and on  $V_2O_5$  catalyst without NO (open symbols) (773 K, 3 kPa  $C_3H_8$ , 10 kPa  $O_2$ , 30–150 cm<sup>3</sup> min<sup>-1</sup>). The balance selectivity corresponds to C1–C3 oxygenates shown in Figure S7. Dashed curves represent best-fits to the form of eq 2.

selectivity as a function of  $C_3H_8$  conversion for different flow rates (30–150 cm³ min<sup>-1</sup>) in an empty reactor with 0.005 kPa NO and on a  $V_2O_5$  catalyst without NO at identical temperature and reactant pressures (773 K, 3 kPa  $C_3H_8$ , 10 kPa  $O_2$ ). Rates on  $V_2O_5$  decreased slightly with increased conversion (Figure 4a), consistent with the inhibition of C–H activation by products such as  $H_2O$  via their adsorption on active lattice oxygens. <sup>67</sup> In contrast, the  $C_3H_8$  activation rates in  $NO_x$ -promoted homogeneous reactions increased with conversion, suggesting a

corresponding increase in the concentration of OH radical species that abstract H-atoms from alkanes.  $^{19}$ 

The homogeneous and heterogeneous systems also exhibit large differences in selectivity trends (Figure 4b), which can be interpreted using the likely sequence of product formation shown in Scheme 5. The selectivity to  $C_3H_6$  product at zero

Scheme 5. Products Formed in Oxidative Conversion of  $C_3H_8$  via (a) All, (b) Secondary, and (c) Primary  $\bullet C_3H_7$  Radicals

(a) 
$$C_{3}H_{8} \xrightarrow{k_{1}} C_{3}H_{6}$$
 $\downarrow k_{3}$ 
 $\downarrow k_{3}$ 

conversion represents the fraction of primary  $C_3H_8$  activations that branch to this product. The decrease in  $C_3H_6$  selectivity with increasing conversion represents sequential conversion of  $C_3H_6$  to secondary products (Scheme 5a). A balance over the moles of products, when their formation rates can be represented by lumped first-order rate constants for parallel conversions of  $C_3H_8$  ( $k_1$ ,  $k_2$ , Scheme 5a) and sequential conversion of  $C_3H_6$  ( $k_3$ ), lead to selectivity at zero conversion ( $S_{C_3H_6}^0$ ) given by derivations in Section S8.1:<sup>68</sup>

$$S_{C_3H_6}^0 = \frac{k_1}{k_1 + k_2} = \frac{1}{1 + \frac{k_2}{k_1}} \tag{1}$$

and the selectivity  $(S_{C_1H_6})$  at finite conversions  $(X_{C_1H_8})$  given by

$$S_{C_3H_6} = \frac{S_{C_3H_6}^0}{\left(1 - S_{C_3H_6}^0 \frac{k_3}{k_1}\right) X_{C_3H_8}} [(1 - X_{C_3H_8})^{S_{C_3H_6}^0 k_3/k_1} - (1 - X_{C_3H_8})]$$
(2)

Regression of  $S_{\rm C_3H_6}$  data in Figure 4b to the form of eqs 1 and 2 provides rate-constant-ratios that represent numerical descriptors of the selectivity trends, where smaller  $k_2/k_1$  and  $k_3/k_1$  values represent higher selectivity at zero conversion and weaker selectivity decrease with increasing conversion, respectively.

For the data shown in Figure 4, the  $k_3/k_1$  values are much smaller in NO<sub>x</sub>-mediated reactions than on V<sub>2</sub>O<sub>5</sub> (2.1 ± 0.19 and 56.7 ± 0.8 for NO<sub>x</sub> and V<sub>2</sub>O<sub>5</sub>, respectively), suggesting that lattice O-atoms of V<sub>2</sub>O<sub>5</sub> favor sequential reactions of C<sub>3</sub>H<sub>6</sub> ( $k_3$ ) over primary C<sub>3</sub>H<sub>8</sub> activations ( $k_1$ ) more than the radicals generated in NO<sub>x</sub>-based pathways. These details are consistent with the weaker allylic C–H bond in C<sub>3</sub>H<sub>6</sub> (bond dissociation enthalpy, BDE, 411 and 363 kJ mol<sup>-1</sup> for CH<sub>3</sub>C<u>H</u><sub>2</sub>CH<sub>3</sub> and CH<sub>2</sub>CHC<u>H</u><sub>3</sub>, respectively; Table 2), the preference of lattice oxygens to activate these weaker bonds (Figure 3) or form C–O bonds in alkenes, and the ability of strong abstractors to dampen

such preference due to formation of early C-H activation transition states (as shown in Scheme 3 and Figure 3).

The NO<sub>x</sub>-mediated reactions exhibit larger  $k_2/k_1$  values than  $V_2O_5$  (0.23  $\pm$  0.01 and 0.08  $\pm$  0.01, respectively, for data in Figure 4) and form significant amounts of C<sub>2</sub>H<sub>4</sub> at zero conversion, instead of CO and CO<sub>2</sub> (Figure 4b). On the basis of the atomic connectivity in the radicals, the C<sub>2</sub>H<sub>4</sub> products can form via C-C bond cleavage in primary ●CH<sub>2</sub>CH<sub>2</sub>CH<sub>3</sub> radicals 69,70 but not in the more stable secondary CH<sub>3</sub>•CHCH<sub>3</sub> radicals resulting from C<sub>3</sub>H<sub>8</sub> activations (Scheme 5b,c; BDE: 422 and 411 kJ mol<sup>-1</sup> for CH<sub>3</sub>CH<sub>2</sub>CH<sub>3</sub> and CH<sub>3</sub>CH<sub>2</sub>CH<sub>3</sub>, respectively, Table 2). Weaker abstractors such as lattice V=O\* species in V<sub>2</sub>O<sub>5</sub> prefer to activate weaker C-H bonds at a much higher rate (Figure 3) and, therefore, form predominantly CH<sub>3</sub>•CHCH<sub>3</sub> radicals that cannot crack to form C<sub>2</sub>H<sub>4</sub>. The •CH<sub>2</sub>CH<sub>2</sub>CH<sub>3</sub> radical formation in NO<sub>x</sub>-mediated homogeneous reactions shows that the OH radicals generated in these routes activate both weak and strong C-H bonds in C<sub>3</sub>H<sub>8</sub> and generate both primary and secondary radicals, which is consistent with the dampening of bond-strength discrimination by OH radicals. The C<sub>2</sub>H<sub>4</sub> selectivity remains near 10% in Figure 4b, which suggests that not all C<sub>3</sub>H<sub>7</sub> radicals formed are primary • CH<sub>2</sub>CH<sub>2</sub>CH<sub>3</sub> radicals and not all of them crack to give C<sub>2</sub>H<sub>4</sub>. A majority of the radicals formed are either CH3•CHCH3 or •CH<sub>2</sub>CH<sub>2</sub>CH<sub>3</sub> radicals that proceed via dehydrogenation or Oinsertion pathways to form oxygenates, with minority cracking products forming from the primary radicals. In contrast, the Oatoms in V<sub>2</sub>O<sub>5</sub> only activate the weaker secondary C-H bond in  $C_3H_8$  to form the secondary radical, which leads to higher  $C_3H_6$ selectivity at zero conversion and lower  $k_2/k_1$  values. Thus, the formation of C<sub>2</sub>H<sub>4</sub> is an important evidence of the involvement of strong abstractors such as •OH radicals in the homogeneous reactions.

The formation of C<sub>2</sub>H<sub>4</sub> via C-C cleavage in primary •CH<sub>2</sub>CH<sub>2</sub>CH<sub>3</sub> radicals also results in •CH<sub>3</sub> radicals (Scheme 5c). These radicals can either form C-O bonds with the O-atom containing gaseous species or couple with other •CH<sub>3</sub> radicals to form C<sub>2</sub>H<sub>6</sub>, and C<sub>2</sub>H<sub>4</sub> upon further dehydrogenation. The coupling of radicals can be tested using ratios of carbon moles in C2 hydrocarbons to C1 products, which should be less than two if no coupling occurred and some C<sub>2</sub>H<sub>4</sub> molecules formed in C-C cleavage steps oxidized further to C1 products. The measured C2 hydrocarbons to C1 product ratios are, however, much greater than two at low residence times, suggesting that significant coupling of •CH3 radicals does occur despite low concentrations of these radicals (details in Section S6 and Figure S9). In contrast, direct coupling products of a primary C<sub>3</sub>H<sub>7</sub> radical with another C<sub>3</sub>H<sub>7</sub> radical or cross coupling with CH<sub>3</sub> radical is not observed. These details are analyzed further by examining the reactive preferences for primary C<sub>3</sub>H<sub>7</sub> and CH<sub>3</sub> radicals via plausible steps shown in Scheme 6 and electronic energy, enthalpy, and free energy of these steps in Table 4.

The cracking of primary radicals •CH<sub>2</sub>CH<sub>2</sub>CH<sub>3</sub> is endothermic but highly exoergic (step 1, Table 4 and Scheme 6), due to entropy gain from the formation of two species from one. This step becomes even more exoergic if radical concentrations are lower than the arbitrary low concentration chosen in Table 4 and if temperatures are higher. In contrast, the coupling steps from propyl radicals (steps 2 and 3, Table 4, Scheme 6) are highly endothermic, but they require entropy loss from formation of a single product to form two species present in very low concentrations, which lead to more free energy penalty for lower pressures and higher temperatures. H-abstraction from

Scheme 6. Products Formed from (a) Primary •C<sub>3</sub>H<sub>7</sub> and (b) •CH<sub>3</sub> Radicals

(a) 
$$\overset{\bullet \text{CH}_2\text{CH}_2\text{CH}_3}{\overset{\bullet}{\smile}} C_3\text{H}_6 + \overset{\bullet}{\smile}\text{OOH}$$

$$\overset{\bullet \text{CH}_2\text{CH}_2\text{CH}_3}{\overset{\bullet}{\smile}} C_4\text{H}_{10} \qquad \overset{\bullet \text{CH}_2\text{CH}_2\text{CH}_3}{\overset{\bullet}{\smile}} C_6\text{H}_{14}$$
(b)  $\overset{\bullet \text{CH}_3}{\overset{\bullet}{\smile}} C_4\text{H}_{10} \qquad \overset{\bullet \text{CH}_3}{\overset{\bullet}{\smile}} C_2\text{H}_2 + \overset{\bullet}{\smile}\text{OOH}$ 

$$\overset{\bullet \text{CH}_3}{\overset{\bullet}{\smile}} C_2\text{H}_6 \qquad \overset{\bullet \text{CH}_3\text{OO}}{\overset{\bullet}{\smile}} C_3\text{H}_6 + \overset{\bullet}{\smile}\text{OOH}$$

primary  $C_3H_7$  radicals is also favored by enthalpy and free energy (step 4, Table 4), and it is very facile with slightly negative electronic activation energy (Figure 3; Figure S14). In contrast to radical coupling, this step also involves reaction of a radical present in low concentrations with an  $O_2$  molecule fed at a much higher concentration leading to a much lower entropy penalty and higher rate compared to coupling reactions with near-zero activation energy but an entropy penalty to bring two species of low concentrations together. These details suggest that, when propyl radicals are present at low concentrations, its cracking and dehydrogenation by  $O_2$  will be preferred over coupling reactions.

In contrast to propyl radicals, methyl radicals contain only one C atom and its reactions must involve coupling or reactions with O<sub>2</sub> (Scheme 6). The electronic energies and free energies in Table 4 show that the coupling of two methyl radicals (step 5) is more favorable than the coupling of two propyl radicals of the cross-coupling (steps 2,3) at the same concentration of all radicals. In contrast, the reactions of methyl radicals with O<sub>2</sub> are much less favorable (steps 6, 7) than such reactions for propyl radicals (step 4). The free energy difference between coupling of two propyl radicals and two methyl radicals is even more positive than the corresponding electronic energies (electronic energy and free energy difference +20 and +45 kJ mol<sup>-1</sup>, respectively, in steps 3 and 5; similar differences exist but are less prominent for cross-coupling). The enthalpy and entropy contributions to these differences are shown in Section S14. The coupling of radicals is highly exothermic, suggesting that it likely proceeds via early transition states with insignificant enthalpy barriers. The Gibbs free energy for activation, however, also involves entropy contributions. The •CH2CH2CH3 radicals exhibit significantly greater rotational entropy than •CH3 radicals leading to more significant entropy loss in the longer chain radicals because of the coupling. This greater entropy loss leads to higher Gibbs free energy and lower coupling preference for •CH<sub>2</sub>CH<sub>2</sub>CH<sub>3</sub> for both self-coupling and cross-coupling because the molecule must align at the transition states to undergo coupling. The secondary propyl radicals are also formed as shown in Scheme 5b, but these species cannot crack and exhibit weaker coupling preferences than primary radials, resulting in their contributions only to dehydrogenation or Oinsertion events. Thus, these energies confirm that methyl radicals have significantly greater preference for coupling over other preferences favored by propyl radicals, consistent with measured selectivity for C2/C1 products and lack of observed C6 and C4 products, which was also observed recently for boron nitride catalysts.7

Table 4. Electronic Energies, Enthalpies, and Gibbs Free Energies at 773 K, Derived from PBE-D3BJ Level of Theory, for Conversions of •C<sub>3</sub>H<sub>7</sub> and •CH<sub>3</sub> Radicals Shown in Scheme 6<sup>a</sup>

no.	reaction	$\Delta E \text{ (kJ mol}^{-1}\text{)}$	$\Delta H (kJ \text{ mol}^{-1})$	$\Delta G$ (kJ mol <sup>-1</sup> )
1	$n - \bullet C_3 H_7 \rightarrow C_2 H_4 + \bullet CH_3$	123	108	-66
2	$n - \bullet C_3H_7 + \bullet CH_3 \rightarrow C_4H_{10}$	-392	-369	-150
3	$2n-\bullet C_3H_7 \rightarrow C_6H_{14}$	-382	-359	-124
4	$n - \bullet C_3H_7 + O_2 \rightarrow C_3H_6 + \bullet OOH$	-62	-63	-82
5	$2 \bullet CH_3 \rightarrow C_2H_6$	-401	-378	-169
6	$\bullet$ CH <sub>3</sub> + O <sub>2</sub> $\rightarrow$ $\bullet$ CH <sub>3</sub> OO	-159	-144	-26
7	$\bullet CH_3 + O_2 \rightarrow CH_2 + \bullet OOH$	260	260	146

<sup>a</sup>Pressures: 0.001 kPa for radical species, 10 kPa for  $O_2$ .

The residence time effects highlight significant differences between reactions at lattice O-atoms and the pathways mediated by strong gas-phase H-abstractors. Next, we further probe these differences by examining the effect of reactant pressures on rates and selectivity.

### 5. EFFECTS OF REACTANT PRESSURES ON RATES AND SELECTIVITY

The effect of  $O_2$  pressure on  $C_3H_8$  activation rates in the 12 cm<sup>3</sup> quartz reactor at different temperatures is shown in Figure 5a

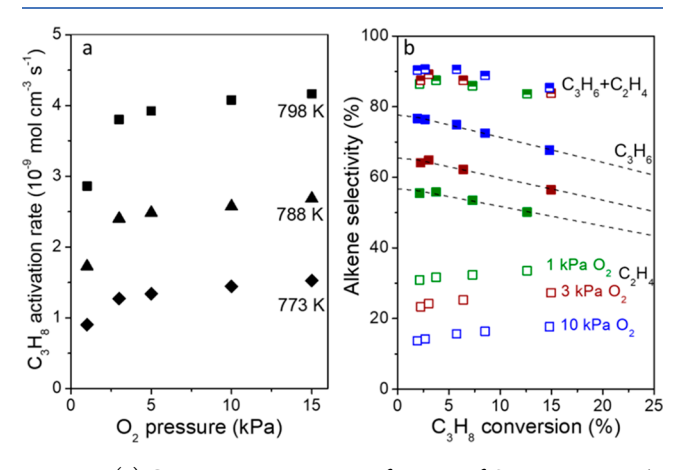


**Figure 5.** (a)  $C_3H_8$  activation rates as a function of  $O_2$  pressure at a 60 cm<sup>3</sup> min<sup>-1</sup> flow rate and at 773, 788, and 798 K, and (b) alkene selectivity as a function of conversion for 30-100 cm<sup>3</sup> min<sup>-1</sup> flow rates at 798 K and 1, 3, and 10 kPa  $O_2$  (0.005 kPa NO, 3 kPa  $C_3H_8$ , 12 cm<sup>3</sup> reactor). Dashed curves represent best-fits to the form of eq 2.

 $(773, 788, \text{ and } 798 \text{ K}; 60 \text{ cm}^3 \text{ min}^{-1}, 0.005 \text{ kPa NO}, 3 \text{ kPa C}_3 \text{H}_8$ 1-15 kPa  $O_2$ ). At each of these temperatures, rates increase with O<sub>2</sub> pressure at pressures less than 5 kPa O<sub>2</sub> but become nearly insensitive to O2 pressure at higher pressures. Figure 5b shows product selectivities as a function of conversion for different O2 pressures at 798 K. Higher O<sub>2</sub> pressures lead to higher C<sub>3</sub>H<sub>6</sub> selectivity and correspondingly lower C<sub>2</sub>H<sub>4</sub> selectivity, such that the sum of C<sub>3</sub>H<sub>6</sub> and C<sub>2</sub>H<sub>4</sub> selectivity remains nearly independent of O<sub>2</sub> pressure (Figure 5b; 798 K). The slopes of trend-lines for the effect of conversion on selectivity are affected less significantly by O2 pressures than the intercepts. These results suggest that higher O<sub>2</sub> pressures increase the C<sub>3</sub>H<sub>8</sub> activation rates slightly (Figure 5a) and exhibit only small effects on the rates of activation of C<sub>3</sub>H<sub>6</sub> relative to C<sub>3</sub>H<sub>8</sub> greatly  $(k_3/k_1)$  values indicated by slopes of dashed curves in Figure 5b). Instead, the most significant effect of O<sub>2</sub> involves altering the branching between C-H activation and C-C bond cleavage in primary •CH<sub>2</sub>CH<sub>2</sub>CH<sub>3</sub> radicals (steps represented by constants

 $k_1''$  and  $k_{2,1}''$  in Scheme 5c). These primary radicals are unstable and undergo a second C–H activation to form  $C_3H_6$  even by weak abstractors such as  $O_2$  (Figure 3). Higher  $O_2$  pressures increase the rate of this bimolecular C–H activation over monomolecular C–C cleavage. Such results are counterintuitive in the light of attempts to improve selectivity on oxide catalysts by staging the  $O_2$  feed to maintain low  $O_2$  concentrations. They also present opportunities for increasing  $C_3H_6$  yields beyond values reported here using  $O_2$  pressures much higher than that required by reaction stoichiometry.

The effect of  $C_3H_8$  pressure on  $C_3H_8$  activation rates in a 12 cm<sup>3</sup> quartz reactor at different temperatures is shown in Figure 6a (773, 788, and 798 K; 60 cm<sup>3</sup> min<sup>-1</sup>, 0.005 kPa NO, 0.6–11

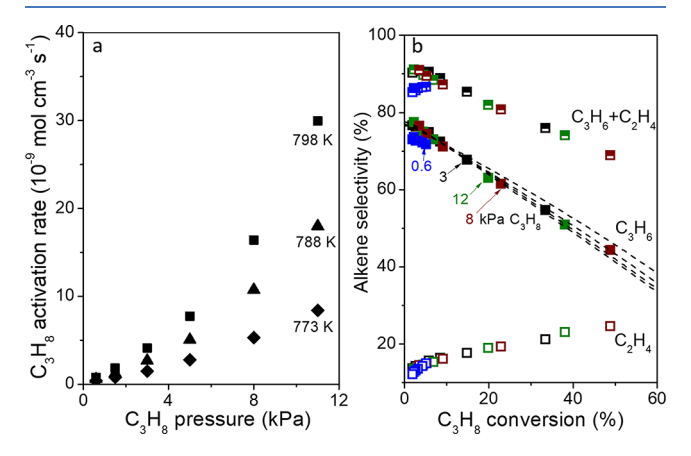


**Figure 6.** (a)  $C_3H_8$  activation rates as a function of  $C_3H_8$  pressure at 60 cm<sup>3</sup> min<sup>-1</sup> flow rate, 773, 788 and 798, and (b) alkene selectivity as a function of conversion for 20–150 cm<sup>3</sup> min<sup>-1</sup> at 798 K, 0.6–12 kPa  $C_3H_8$  (0.005 kPa NO, 10 kPa  $O_2$ , 12 cm<sup>3</sup> reactor). Dashed curves represent best-fits to the form of eq 2.

kPa  $C_3H_8$ , 10 kPa  $O_2$ ).  $C_3H_8$  activation rates exhibit a supralinear increase with  $C_3H_8$  pressure, suggesting that higher alkane concentrations increase concentrations of OH radicals that activate alkanes because more sacrificial species for activating  $NO_2$  (step 2, Schemes 1 and 4) and more  $H_2O$  is present at a given conversion when the alkane pressure is higher. Figure 6b shows that  $C_3H_6$  and  $C_2H_4$  selectivities remain nearly independent of  $C_3H_8$  pressure above 3 kPa at 798 K.

The effect of  $\rm H_2O$  pressure from  $\rm H_2O$  cofed with reactants and formed from  $\rm C_3H_8-O_2$  conversions on rates and selectivity are shown in Figure 7. The reaction rates increase significantly with added  $\rm H_2O$  pressure (Figure 7a), as also shown by increasing conversions in Figure 2. The rate enhancements by added  $\rm H_2O$  are much more significant at higher temperature (Figure 7a; 773 and 798 K, 30 cm³ min<sup>-1</sup>, 0.005 kPa NO, 0–10

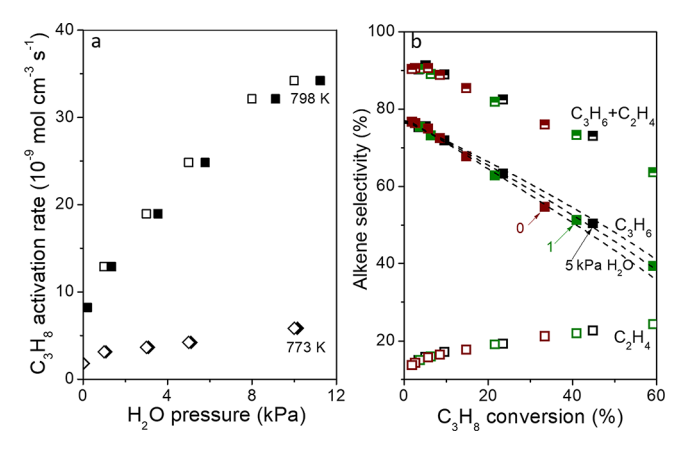


**Figure 7.** (a)  $C_3H_8$  activation rates as a function of added  $H_2O$  pressure (open symbols) and sum of added and formed  $H_2O$  pressure (closed symbols) at 30 cm<sup>3</sup> min<sup>-1</sup> flow rate, 773, and 798 K, and (b) alkene selectivity as a function of conversion for 20-100 cm<sup>3</sup> min<sup>-1</sup> at 798 K, 0-5 kPa added  $H_2O$  (0.005 kPa NO, 3 kPa  $C_3H_8$ , 10 kPa  $O_2$ , 12 cm<sup>3</sup> reactor). Dashed curves represent best-fits to the form of eq 2.

kPa  $\rm H_2O$ , 3 kPa  $\rm C_3H_8$ , 10 kPa  $\rm O_2$ ).  $\rm H_2O$  formed from the reaction shifts the trends only slightly, and the nonzero intercepts in these trends suggest that rate enhancement form  $\rm NO_x$  catalysis, which is further enhanced by  $\rm H_2O$ . These results are consistent with the role of  $\rm H_2O$  in forming HONO from NO and  $\rm NO_2$  in proposed mechanisms (Schemes 1 and 4), and the facile nature of these steps reported form experimental studies in literature. <sup>65,66</sup> Figure 7b shows product selectivities as a function of conversion for added  $\rm H_2O$  pressures at 798 K. The  $\rm C_3H_6$  and  $\rm C_2H_4$  selectivities remain nearly independent of added  $\rm H_2O$  (Figure 7b).

These effects of reactant pressures deviate significantly from ODH reactions on oxide catalysts that involve MvK cycles with rate-limiting C–H activation at lattice O-atoms of oxides and fast  $O_2$  activation. <sup>41</sup> Such mechanisms invariably exhibit a first-order dependence on alkane pressure and zero-order dependence on  $O_2$  pressure. <sup>1,72–75</sup> The ODH rates in MvK cycles show a small decrease in rates with  $H_2O$  pressures due to its adsorption at active sites. <sup>1,67</sup> The results in  $NO_x$ -mediated reactions (Figures 5–7) and their deviations from heterogeneous reactions on oxides are also observed in trends reported recently for boron nitride <sup>6,11</sup> and previously for systems in which catalysts generate radicals for homogeneous reactions; <sup>5</sup> they likely originate here from higher concentrations of  $\bullet OH$  species in  $NO_x$ -mediated routes at higher alkane,  $O_2$ , and  $H_2O$  pressures (Schemes 1 and S3; Supporting Information).

The  $C_3H_6$  selectivity data as a function of conversion for the different reactant pressures and reaction temperatures shown in Figures 5–7 and Figure S11 are regressed to the form of eq 2 to determine rate constant ratios, which are shown as a function of reactant pressures and reciprocal temperature in Figures 8 and 9, respectively. These data are used to summarize the effect of reactant pressure on selectivity and derive activation energy differences relevant to selectivity via effects of temperature on the ratios.

Figure 8 shows the rate constant ratios as a function of reactant pressures.  $C_3H_8$  and  $H_2O$  pressures do not have significant effects on  $k_2/k_1$  values (Figure 8a). Higher  $O_2$  pressures lead to much smaller  $k_2/k_1$  values, which correspond to lesser C-C cleavage and greater  $C_3H_6$  selectivity (Figure 5b). These effects suggest that primary  $\bullet C_3H_7$  species responsible for  $C_2H_4$  formation undergo C-H activation more preferentially

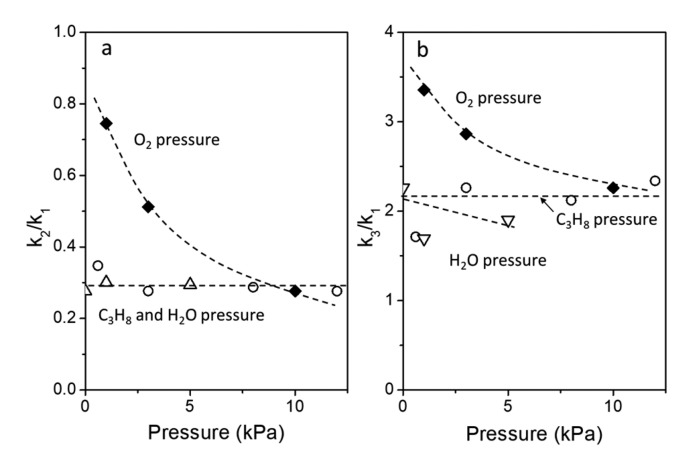


**Figure 8.** Ratios of rate constants (a)  $k_2/k_1$  and (b)  $k_3/k_1$ , as a function of  $C_3H_8$  pressure (circles, 10 kPa  $O_2$ , 0 kPa  $H_2O$ ),  $O_2$  pressure (diamonds, 3 kPa  $C_3H_8$ , 0 kPa  $H_2O$ ), and  $H_2O$  pressure (triangles, 3 kPa  $C_3H_8$ , 10 kPa  $O_2$ ) at 798 K and 0.005 kPa NO. Dashed curves represent trends.

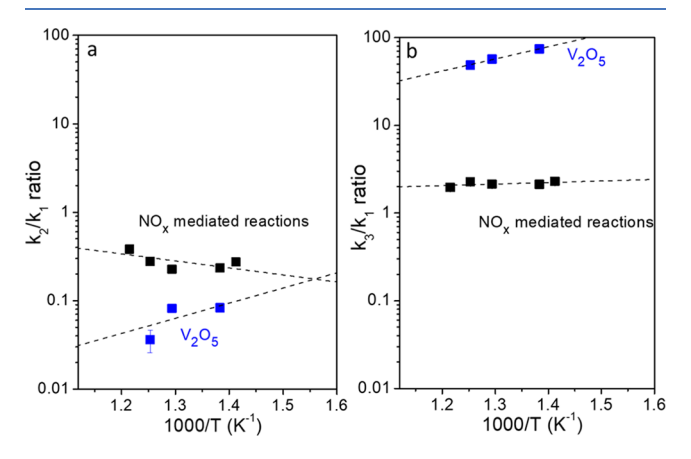


**Figure 9.** Ratios of rate constants (a)  $k_2/k_1$  and (b)  $k_3/k_1$ , as a function of reciprocal temperature at 0.005 kPa NO, 3 kPa  $C_3H_8$ , and 10 kPa  $O_2$ . Dashed lines represent exponential best-fits for the values. Uncertainties represent standard errors.

than C–C activation when more  $O_2$  is present (Scheme 5c). The  $k_3/k_1$  values are nearly unaffected by  $C_3H_8$  or  $H_2O$  pressures (Figure 8b) but decrease slightly (implying higher selectivity) at higher  $O_2$  pressure. These data suggest that using denser feeds with high alkane and  $H_2O$  pressures will significantly enhance the rates (Figures 6a and 7a) and productivity (Table S2), while retaining high selectivity and yields. Furthermore, high  $O_2$  pressures can be used to decrease  $C_2H_4$  selectivity and increase  $C_3H_6$  selectivity to values higher than that shown here (Figure 5b).

# 6. EFFECT OF ABSTRACTOR STRENGTH ON ACTIVATION ENTHALPY DIFFERENCES FOR STEPS INVOLVING C—H BONDS OF DIFFERENT STRENGTHS

Figure 9 shows the rate constant ratios  $k_2/k_1$  and  $k_3/k_1$ , representing selectivity for  $C_3H_6$  formation over parallel and sequential reactions, respectively, as a function of reciprocal temperature for identical reactant pressures on  $V_2O_5$  catalyst and in  $NO_x$ -catalyzed reactions.  $NO_x$ -mediated reactions exhibit larger  $k_2/k_1$  values than  $V_2O_5$  (Figure 9a) because generation of primary radicals leads to significant C–C bond cleavage, which

results in high  $C_2H_4$  selectivity at zero conversion (Figure 4b). The  $k_3/k_1$  values are much larger in  $V_2O_5$  than in  $NO_x$ -mediated reactions because the latter reactions dampen the secondary reactions of  $C_3H_6$  (Figure 9b).

The effects of temperature on rate constant ratios, at identical reactant pressures in Figure 9 ( $k_2/k_1$ , and  $k_3/k_1$  at 0.005 kPa NO, 3 kPa C<sub>3</sub>H<sub>8</sub>, and 10 kPa O<sub>2</sub>), are expressed as activation enthalpy differences between the parallel or sequential undesired reactions and the C<sub>3</sub>H<sub>6</sub> formation reaction using the following relations (details in section S8.2):

$$\frac{k_2}{k_1} = \exp\left(\frac{\Delta S_2^{\text{act}} - \Delta S_1^{\text{act}}}{R}\right) \exp\left(-\frac{\Delta H_2^{\text{act}} - \Delta H_1^{\text{act}}}{RT}\right)$$

$$= \exp\left(\frac{\Delta \Delta S_{21}}{R}\right) \exp\left(-\frac{\Delta \Delta H_{21}}{RT}\right)$$

$$\frac{k_3}{k_1} = \exp\left(\frac{\Delta S_3^{\text{act}} - \Delta S_1^{\text{act}}}{R}\right) \exp\left(-\frac{\Delta H_3^{\text{act}} - \Delta H_1^{\text{act}}}{RT}\right)$$

$$= \exp\left(\frac{\Delta \Delta S_{31}}{R}\right) \exp\left(-\frac{\Delta \Delta H_{31}}{RT}\right)$$
(4)

where,  $\Delta H_1^{\rm act}$  and  $\Delta H_2^{\rm act}$  represent ensemble averaged activation enthalpy for  $C_3H_6$  formation and all steps mediating parallel  $C_3H_8$  oxidation steps relative to gaseous  $C_3H_8$  (Scheme 5a), respectively,  $\Delta H_3^{\rm act}$  represents activation enthalpy for  $C_3H_6$  oxidation steps relative to gaseous  $C_3H_6$ , and  $\Delta S^{\rm act}$  values represent corresponding activation entropies. The values of activation enthalpy differences relevant to rate constant ratios  $k_2/k_1$  ( $\Delta\Delta H_{21}=\Delta H_2^{\rm act}-\Delta H_1^{\rm act}$ ) and  $k_3/k_1$  ( $\Delta\Delta H_{31}=\Delta H_3^{\rm act}-\Delta H_1^{\rm act}$ ) derived from slopes of regressed lines in Figure 9 are shown in Table 5.

Table 5. Activation Enthalpy Differences between the Parallel or Sequential Reactions and the Primary C-H Activations Derived from Regression of Rate Constants Ratios in Figure 9 to the Form of eqs 3 and  $4^a$ 

reaction system	$\Delta H_2^{\rm act} - \Delta H_1^{\rm act}$ (kJ mol <sup>-1</sup> )	$\Delta H_3^{\rm act} - \Delta H_1^{\rm act}  (\text{kJ mol}^{-1})$
$V_2O_5$	$-33 \pm 34$	$-26 \pm 1$
$NO_x$ -mediated	$15 \pm 10$	$-3 \pm 3$

<sup>&</sup>lt;sup>a</sup>Uncertainties represent the standard errors.

The rate constant ratios on the V<sub>2</sub>O<sub>5</sub> catalyst decrease with increasing temperature (Figure 9), suggesting that the activation enthalpy for parallel and sequential undesired reactions are lower than the primary reaction in Scheme 5a ( $\Delta\Delta H_{21} = -33 \pm$ 34 kJ mol<sup>-1</sup> and  $\Delta \Delta H_{31} = -26 \pm 1$  kJ mol<sup>-1</sup>; Table 5). In contrast, NO<sub>x</sub>-mediated homogeneous reactions exhibit increasing  $k_2/k_1$  values with temperature, which shows that the activation enthalpy for the C<sub>2</sub>H<sub>4</sub> formation step is higher than for the C-H activation in  $C_3H_8$  ( $\Delta\Delta H_{21} = 15 \pm 10 \text{ kJ mol}^{-1}$ ; Table 5). The  $C_2H_4$  formation step can only occur via C-C cleavage in primary •C<sub>3</sub>H<sub>7</sub> radicals (Scheme 5c), suggesting that NO<sub>x</sub> reactions involve significant formation of such primary radicals, in spite of the stronger C-H bonds involved in forming these radicals (Table 2). The activation of primary and secondary C-H bonds in C<sub>3</sub>H<sub>8</sub> cannot be differentiated from Figure 9, because the  $k_1$  values represent an ensemble average of all C-H activations occurring in C<sub>3</sub>H<sub>8</sub>. Therefore, the positive  $\Delta\Delta H_{21}$  values indicate that the C–C bond cleavage in primary

 $\bullet$ C<sub>3</sub>H<sub>7</sub> radical, which does not involve strong H-abstractors, has higher activation enthalpy than the C-H activation required to form this radical.

The  $k_3/k_1$  values in NO<sub>x</sub> reactions are much lower than V<sub>2</sub>O<sub>5</sub> and exhibit a much weaker temperature dependence ( $\Delta \Delta H_{31}$  =  $-3 \pm 3$  and  $-26 \pm 1$  kJ mol<sup>-1</sup> for NO<sub>x</sub> and V<sub>2</sub>O<sub>5</sub>, respectively; Table 5). The steps for  $C_3H_6$  reactions involve kinetically relevant activation of weak allylic C-H bonds prior to C-O bond formation that leads to oxygenates. <sup>49,76</sup> Therefore,  $\Delta\Delta H_{31}$ represents activation enthalpy differences for C-H activation in C<sub>3</sub>H<sub>6</sub> and C<sub>3</sub>H<sub>8</sub>, and its negative values indicate that C<sub>3</sub>H<sub>6</sub> activation is more facile due to weaker C-H bonds (Table 2). However, the  $\Delta \Delta H_{31}$  values in NO<sub>x</sub> reactions are much closer to zero than V<sub>2</sub>O<sub>5</sub>, which means that the H-abstractors involved in NO<sub>x</sub>-mediated reactions can activate the two bonds with only slightly different rates despite the large difference in bond strength. This difference between C<sub>3</sub>H<sub>8</sub> and C<sub>3</sub>H<sub>6</sub> activation energies derived from DFT is described next for C-H activation using the H-abstractors of different strengths shown in Table 1.

Figure 10 shows the DFT-derived difference between electronic energies for C-H activation at a secondary C-H

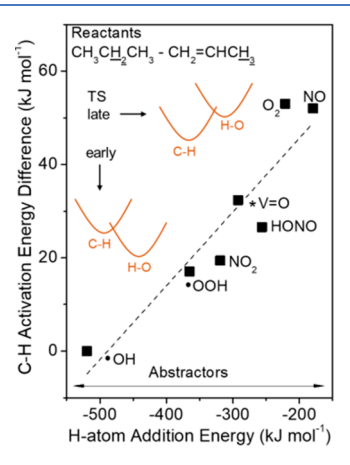


**Figure 10.** DFT-derived C-H activation energy differences between  $C_3H_8$  and  $C_3H_6$  as a function of HAE on different H-abstractors.

bond in C<sub>3</sub>H<sub>8</sub> (BDE 411 kJ mol<sup>-1</sup>, Table 2) and an allylic C-H bond in C<sub>3</sub>H<sub>6</sub> (BDE 363 kJ mol<sup>-1</sup>, Table 2) as a function of the HAE of H-abstractors. When the abstractor is weak (less negative HAE; e.g., NO in Table 1), the product state is less stable than the reactant. This scenario can be shown using a crossing potential for C-H cleavage and O-H formation, in which the product O-H potential is higher in energy than the reactant (inset in Figure 10). Such cases lead to high activation energies and the transition state represented by the crossing point of the potentials is "late" because it requires nearly full cleavage of the C-H bond and formation of the O-H bond. The lateness is to be confirmed by the structures and energies of transition states shown in Section S13. Such late transition states are highly sensitive to C-H bond strength, because the bond is nearly broken at the transition state. As a result, the C-H activation energy is very different in the stronger C<sub>3</sub>H<sub>8</sub> C-H bond and the weaker C<sub>3</sub>H<sub>6</sub> C-H bond. However, when the abstractor is strong (more negative HAE; e.g., OOH and OH in Table 1), the product state potential shifts to lower energies and leads to "early" transition states. Very early transition states do not involve significant C-H bond stretching and are insensitive to the C-H bond strength, leading to small differences between activation energy for strong and weak bonds in Figure 10. Thus,

the DFT-derived energies confirm that strong abstractors would lead to improvement in selectivity by suppression of bond-strength effects. Notably, the activation energy difference is fairly significant for  $V_2O_5$  O-atoms (+32 kJ mol<sup>-1</sup>, Figure 10), and even for OOH radicals (+17 kJ mol<sup>-1</sup>, Figure 10), suggesting that only OH radicals, the strongest abstractor among those shown in Figure 10, can account for the  $\Delta\Delta H_{31}$  values near zero in the measured data ( $\Delta\Delta H_{31} = -3 \pm 3$  kJ mol<sup>-1</sup>, Table 5).

Thus, we conclude that the generation of OH radicals for C-H activation and the dampening of bond-strength discrimination by such strong abstractors lead to high selectivity and yield for alkenes. The OH radicals generated in NO<sub>x</sub>-mediated reaction paths abstract both primary and secondary C-H bonds in C<sub>3</sub>H<sub>8</sub>. The primary alkyl radicals can undergo C-C bond cleavage, which leads to significant C<sub>2</sub>H<sub>4</sub> formation in addition to the dehydrogenation product C<sub>3</sub>H<sub>8</sub>. The yields attained in this process are shown in Table S1 and Figure S1, along with yields reported in the literature. At 798 K, 24% maximum C<sub>3</sub>H<sub>6</sub> yield was attained, and the corresponding maximum alkene  $(C_3H_6 + C_2H_4)$  and alkene + C3-oxygenates yields are 43% and 47%, respectively. An important consequence of strong abstractors and the low activation energy differences is that the yields are quite insensitive to temperature. As a result, the C<sub>3</sub>H<sub>6</sub> yields >22% are attained even at temperatures much lower than previously reported in any other systems (723 K, Figure S1). These lower temperature conditions lead to a lower fraction of C<sub>2</sub>H<sub>4</sub> (combined C<sub>3</sub>H<sub>6</sub>+C<sub>2</sub>H<sub>4</sub> yield 31%) with a greater fraction of additional valuable C3 oxygenate products that are not observed in other systems. The lower C-C cleavage at lower temperature  $(k_2/k_1, \text{Figure 9})$  corresponds to increased fractions of C3 oxygenate (Figure S1) without affecting C<sub>3</sub>H<sub>6</sub> yields and leads to a combined alkene and C3 oxygenate yields of 40% at

The NO $_x$  mediation can also enhance other reactions limited by C–H bond activation. Examples of such reactions shown in Section S15 include: (i) C $_2$ H $_6$  dehydrogenation with high C $_2$ H $_4$  selectivity and (ii) formation of C3 hydrocarbons via C–C coupling in C $_2$ H $_4$ –CH $_3$ OH–O $_2$ –NO reactions. Such facile C–H activations may also be useful for other reactions such as C–C coupling or oxygenate formations that require organic radical intermediates formed via rate-limiting C–H activation steps.  $^{2,77-80}$ 

#### 7. CONCLUSIONS

 $\mathrm{NO}_x$ -mediated generation of OH radical species selectively activates strong C–H bonds in alkanes with high alkene productivity and yields at moderate temperatures by weakening the bond-strength-based discrimination of activation rates. The kinetic details and selectivity trends in these reactions resemble boron nitride and alkali promoted oxides that facilitate homogeneous reactions  $^{5,6,13}$  but differ markedly from reactions at lattice oxygens of oxide catalysts.  $\mathrm{NO}_x$  helps overcome the high temperature requirements for the generation of OH radicals in alkali-based catalysts  $^{5,34,45}$  and, in turn, produces alkyl radicals and dehydrogenated products more efficiently.

#### ASSOCIATED CONTENT

#### S Supporting Information

The Supporting Information is available free of charge on the ACS Publications website at DOI: 10.1021/acscatal.9b03862.

Alkene yields and productivities; methods; definitions of rates and selectivity; effects of time on stream, conversion and reactant pressures, temperatures and reactor volumes on rates and selectivity; C2/C1 selectivity ratios; plausible elementary steps; selectivity trends derivations; structures and energies of transition states;  $C_2H_6$  activation and C-C coupling in  $C_2H_4-CH_3OH-O_2-NO$  reactions (PDF)

#### AUTHOR INFORMATION

#### **Corresponding Author**

\*E-mail: prashant.deshlahra@tufts.edu.

#### ORCID ®

Leelavathi Annamalai: 0000-0001-8207-1424 Prashant Deshlahra: 0000-0002-1063-4379

#### **Notes**

The authors declare no competing financial interest.

#### ACKNOWLEDGMENTS

We are grateful to Prof. Maria Flytzani-Stephanopoulos (Tufts) and Dr. Alon Grinberg Dana (MIT) for helpful discussions and comments on this manuscript. Financial support was provided by Tufts University and National Science Foundation Grant 1803798. Computational resources were provided by Extreme Science and Engineering Discovery Environment (XSEDE), 81 which is supported by National Science Foundation (Grant ACI-1548562).

#### REFERENCES

- (1) Chen, K.; Bell, A. T.; Iglesia, E. Kinetics and Mechanism of Oxidative Dehydrogenation of Propane on Vanadium, Molybdenum, and Tungsten Oxides. *J. Phys. Chem. B* **2000**, *104*, 1292–1299.
- (2) Labinger, J. A.; Bercaw, J. E. Understanding and Exploiting C-H Bond Activation. *Nature* **2002**, *417*, 507.
- (3) Burch, R.; Crabb, E. M. Homogeneous and Heterogeneous Contributions to the Oxidative Dehydrogenation of Propane on Oxide Catalysts. *Appl. Catal.*, A 1993, 100, 111–130.
- (4) Leveles, L.; Fuchs, S.; Seshan, K.; Lercher, J. A.; Lefferts, L. Oxidative Conversion of Light Alkanes to Olefins Over Alkali Promoted Oxide Catalysts. *Appl. Catal., A* **2002**, 227, 287–297.
- (5) Leveles, L.; Seshan, K.; Lercher, J. A.; Lefferts, L. Oxidative Conversion of Propane over Lithium-Promoted Magnesia Catalyst: I. Kinetics and Mechanism. *J. Catal.* **2003**, *218*, 296–306.
- (6) Grant, J. T.; Carrero, C. A.; Goeltl, F.; Venegas, J.; Mueller, P.; Burt, S. P.; Specht, S. E.; McDermott, W. P.; Chieregato, A.; Hermans, I. Selective Oxidative Dehydrogenation of Propane to Propene using Boron Nitride Catalysts. *Science* **2016**, *354*, 1570–1573.
- (7) Grant, J. T.; McDermott, W. P.; Venegas, J. M.; Burt, S. P.; Micka, J.; Phivilay, S. P.; Carrero, C. A.; Hermans, I. Boron and Boron-Containing Catalysts for the Oxidative Dehydrogenation of Propane. *ChemCatChem* **2017**, *9*, 3623–3626.
- (8) Huang, R.; Zhang, B.; Wang, J.; Wu, K. H.; Shi, W.; Zhang, Y.; Liu, Y.; Zheng, A.; Schlögl, R.; Su, D. S. Direct Insight into Ethane Oxidative Dehydrogenation over Boron Nitrides. *ChemCatChem* **2017**, *9*, 3293–3207
- (9) Fang, Y.; Wang, X. Metal-Free Boron-Containing Heterogeneous Catalysts. *Angew. Chem., Int. Ed.* **2017**, *56*, 15506–15518.
- (10) Chaturbedy, P.; Ahamed, M.; Eswaramoorthy, M. Oxidative Dehydrogenation of Propane over a High Surface Area Boron Nitride Catalyst: Exceptional Selectivity for Olefins at High Conversion. *ACS Omega* **2018**, *3*, 369–374.
- (11) Shi, L.; Wang, D.; Song, W.; Shao, D.; Zhang, W. P.; Lu, A. H. Edge-Hydroxylated Boron Nitride for Oxidative Dehydrogenation of Propane to Propylene. *ChemCatChem* **2017**, *9*, 1788–1793.
- (12) Shi, L.; Yan, B.; Shao, D.; Jiang, F.; Wang, D.; Lu, A.-H. Selective Oxidative Dehydrogenation of Ethane to Ethylene over a Hydroxylated Boron Nitride Catalyst. *Chin. J. Catal.* **2017**, *38*, 389–395.

(13) Wang, Y.; Li, W.-C.; Zhou, Y.-X.; Lu, R.; Lu, A.-H. Boron Nitride Wash-Coated Cordierite Monolithic Catalyst Showing High Selectivity and Productivity for Oxidative Dehydrogenation of Propane. *Catal. Today* **2018**, DOI: 10.1016/j.cattod.2018.12.028.

- (14) Yan, B.; Li, W.-C.; Lu, A.-H. Metal-Free Silicon Boride Catalyst for Oxidative Dehydrogenation of Light Alkanes to Olefins with High Selectivity and Stability. *J. Catal.* **2019**, *369*, 296–301.
- (15) Venegas, J. M.; Hermans, I. The Influence of Reactor Parameters on the Boron Nitride-Catalyzed Oxidative Dehydrogenation of Propane. *Org. Process Res. Dev.* **2018**, 22, 1644–1652.
- (16) Otsuka, K.; Takahashi, R.; Yamanaka, I. Oxygenates from Light Alkanes Catalyzed by  $NO_x$  in the Gas Phase. *J. Catal.* **1999**, *185*, 182–191.
- (17) Sen, A.; Lin, M.  $NO_x$ -Catalyzed Partial Oxidation of Methane and Ethane to Formaldehyde by Dioxygen. *Top. Catal.* **2005**, 32, 175–178.
- (18) Frassoldati, A.; Faravelli, T.; Ranzi, E. Kinetic Modeling of the Interactions Between NO and Hydrocarbons at High Temperature. *Combust. Flame* **2003**, *135*, 97–112.
- (19) Zalc, J. M.; Green, W. H.; Iglesia, E. NO<sub>x</sub>-Mediated Homogeneous Pathways for the Synthesis of Formaldehyde from CH<sub>4</sub>-O<sub>2</sub> Mixtures. *Ind. Eng. Chem. Res.* **2006**, 45, 2677–2688.
- (20) Zhang, J.; Burklé-Vitzthum, V.; Marquaire, P. NO<sub>2</sub>-Promoted Oxidation of Methane to Formaldehyde at Very Short Residence Time. Part I: Experimental Results. *Chem. Eng. J.* **2012**, *189*, 393–403.
- (21) Yan, Z.; Xiao, C.-X.; Kou, Y. NO<sub>x</sub>-Catalyzed Gas-Phase Activation of Methane: In Situ IR and Mechanistic Studies. *Catal. Lett.* **2003**, *85*, 135–138.
- (22) Löffler, G.; Wargadalam, V. J.; Winter, F.; Hofbauer, H. Chemical Kinetic Modelling of the Effect of NO on the Oxidation of CH<sub>4</sub> under Fluidized Bed Combustor Conditions. *Fuel* **2002**, *81*, 855–860.
- (23) Glarborg, P.; Alzueta, M.; Kjærgaard, K.; Dam-Johansen, K. Oxidation of Formaldehyde and its Interaction with Nitric Oxide in a Flow Reactor. *Combust. Flame* **2003**, *132*, 629–638.
- (24) Bendtsen, A. B.; Glarborg, P.; Dam-Johansen, K. Low Temperature Oxidation of Methane: The Influence of Nitrogen Oxides. *Combust. Sci. Technol.* **2000**, *151*, 31–71.
- (25) Teng, Y.; Sakurai, H.; Tabata, K.; Suzuki, E. Methanol Formation from Methane Partial Oxidation in CH<sub>4</sub>-O<sub>2</sub>-NO Gaseous Phase at Atmospheric Pressure. *Appl. Catal., A* **2000**, 190, 283–289.
- (26) Otsuka, K.; Takahashi, R.; Amakawa, K.; Yamanaka, I. Partial Oxidation of Light Alkanes by NO<sub>x</sub> in the Gas Phase. *Catal. Today* 1998, 45, 23–28
- (27) Takemoto, T.; Tabata, K.; Teng, Y.; Yao, S.; Nakayama, A.; Suzuki, E. Optimization of  $C_1$ -Oxygenates for the Selective Oxidation of Methane in a Gas-Phase Reaction of  $CH_4$ - $O_2$ -NO at Atmospheric Pressure. *Energy Fuels* **2001**, *15*, 44–51.
- (28) Control of Nitrogen Oxide Emissions: Selective Catalytic Reduction (SCR), Topical Report No. 9; U.S. Department of Energy and Southern Company Service and American Chemical Society, 1997.
- (29) Cox, L. Nitrogen Oxides ( $NO_x$ ) Why and How They Are Controlled, EPA-456/F-99-006R; NTIS: Springfield, VA, 1999.
- (30) Cuffe, S. T.; Gerstle, R. W.; Orning, A. A.; Schwartz, C. H. Air Pollutant Emissions from Coal-Fired Power Plants Report No. 1. *J. Air Pollut. Control Assoc.* **1964**, *14*, 353–362.
- (31) Battye, R.; Walsh, S.; Lee-Greco, J.  $NO_x$  Control Technologies for the Cement Industry (Final Report. EPA Contract No. 68-D98-026; EC/R Incorporated, Chapel Hill, NC, 2000.
- (32) Zabarnick, S. Laser-Induced Fluorescence Diagnostics and Chemical Kinetic Modeling of a CH<sub>4</sub>/NO<sub>2</sub>/O<sub>2</sub> Flame at 55 Torr. *Combust. Flame* **1991**, *85*, 27–50.
- (33) Takanabe, K.; Khan, A. M.; Tang, Y.; Nguyen, L.; Ziani, A.; Jacobs, B. W.; Elbaz, A. M.; Sarathy, S. M.; Tao, F. Integrated In Situ Characterization of a Molten Salt Catalyst Surface: Evidence of Sodium Peroxide and Hydroxyl Radical Formation. *Angew. Chem., Int. Ed.* **2017**, *56*, 10403–10407.
- (34) Takanabe, K.; Shahid, S. Dehydrogenation of Ethane to Ethylene via Radical Pathways Enhanced by Alkali Metal Based Catalyst in Oxysteam Condition. *AIChE J.* **2017**, *63*, 105–110.

(35) Deshlahra, P.; Iglesia, E. Reactivity and Selectivity Descriptors for the Activation of C-H Bonds in Hydrocarbons and Oxygenates on Metal Oxides. *J. Phys. Chem. C* **2016**, *120*, 16741–16760.

- (36) Atkinson, R.; Baulch, D.; Cox, R.; Crowley, J.; Hampson, R.; Hynes, R.; Jenkin, M.; Rossi, M.; Troe, J. Evaluated Kinetic and Photochemical Data for Atmospheric Chemistry: Volume I-Gas Phase Reactions of O<sub>x</sub>, HO<sub>x</sub>, NO<sub>x</sub> and SO<sub>x</sub> species. *Atmos. Chem. Phys.* **2004**, *4*, 1461–1738.
- (37) Beckers, H.; Zeng, X.; Willner, H. Intermediates Involved in the Oxidation of Nitrogen Monoxide: Photochemistry of the cis- $N_2O_2$ . $O_2$  complex and of sym- $N_2O_4$  in Solid Ne Matrices. *Chem. Eur. J.* **2010**, 16, 1506–1520.
- (38) Gadzhiev, O. B.; Ignatov, S. K.; Razuvaev, A. G.; Masunov, A. E. Quantum Chemical Study of Trimolecular Reaction Mechanism Between Nitric Oxide and Oxygen in the Gas Phase. *J. Phys. Chem. A* **2009**, *113*, 9092–9101.
- (39) Maestri, M.; Iglesia, E. First-Principles Theoretical Assessment of Catalysis by Confinement: NO-O<sub>2</sub> Reactions within Voids of Molecular Dimensions in Siliceous Crystalline Frameworks. *Phys. Chem. Chem. Phys.* **2018**, *20*, 15725–15735.
- (40) McKee, M. L. Ab initio Study of the  $N_2O_4$  Potential Energy Surface. Computational Evidence for a New  $N_2O_4$  Isomer. *J. Am. Chem. Soc.* **1995**, *117*, 1629–1637.
- (41) Mars, P.; van Krevelen, D. W. Oxidations Carried Out by Means of Vanadium Oxide Catalysts. *Chem. Eng. Sci.* **1954**, *3*, 41–59.
- (42) Chen, K.; Khodakov, A.; Yang, J.; Bell, A. T.; Iglesia, E. Isotopic Tracer and Kinetic Studies of Oxidative Dehydrogenation Pathways on Vanadium Oxide Catalysts. *J. Catal.* **1999**, *186*, 325–333.
- (43) Grant, J. T.; Venegas, J. M.; McDermott, W. P.; Hermans, I. Aerobic Oxidations of Light Alkanes Over Solid Metal Oxide Catalysts. *Chem. Rev.* **2018**, *118*, 2769–2815.
- (44) Carrero, C.; Schlögl, R.; Wachs, I.; Schomaecker, R. Critical Literature Review of the Kinetics for the Oxidative Dehydrogenation of Propane Over Well-Defined Supported Vanadium Oxide Catalysts. *ACS Catal.* **2014**, *4*, 3357–3380.
- (45) Takanabe, K.; Khan, A. M.; Tang, Y.; Nguyen, L.; Ziani, A.; Jacobs, B. W.; Elbaz, A. M.; Sarathy, S. M.; Tao, F. Integrated In Situ Characterization of a Molten Salt Catalyst Surface: Evidence of Sodium Peroxide and Hydroxyl Radical Formation. *Angew. Chem.* **2017**, *129*, 10539–10543.
- (46) Grimme, S.; Ehrlich, S.; Goerigk, L. Effect of the Damping Function in Dispersion Corrected Density Functional Theory. *J. Comput. Chem.* **2011**, 32, 1456–1465.
- (47) Luo, Y.-R. Comprehensive Handbook of Chemical Bond Energies; CRC Press, Boca Raton, FL, 2007.
- (48) Pudar, S.; Oxgaard, J.; Chenoweth, K.; Van Duin, A. C.; Goddard, W. A. Mechanism of Selective Oxidation of Propene to Acrolein on Bismuth Molybdates from Quantum Mechanical Calculations. *J. Phys. Chem. C* **2007**, *111*, 16405–16415.
- (49) Getsoian, A. B.; Shapovalov, V.; Bell, A. T. DFT+U Investigation of Propene Oxidation over Bismuth Molybdate: Active Sites, Reaction Intermediates, and the Role of Bismuth. *J. Phys. Chem. C* **2013**, *117*, 7123–7137.
- (50) Dozono, T.; Thomas, D.; Wise, H. Mechanism of [3–13 C] Propene Ammoxidation on Bismuth Molybdate Catalyst. *J. Chem. Soc., Faraday Trans.* 1 1973, 69, 620–623.
- (51) Voge, H.; Wagner, C.; Stevenson, D. Mechanism of Propylene Oxidation over Cuprous Oxide. *J. Catal.* **1963**, *2*, 58–62.
- (52) Tsang, W. Chemical Kinetic Data Base for Combustion Chemistry. Part 3: Propane. J. Phys. Chem. Ref. Data 1988, 17, 887–951.
- (53) Titarchuk, T. A.; Ballod, A. P.; Shtern, V. Y. Rate Constant of Generation of Isopropyl Radicals During Thermal Nitration of Propane by Nitrogen-Dioxide. *Kinet. Catal.* **1976**, *17*, 932–932.
- (54) Baldwin, R. R.; Walker, R. W. Rate Constants for Hydrogen +Oxygen System, and for H Atoms and OH Radicals+Alkanes. *J. Chem. Soc., Faraday Trans. 1* **1979**, *75*, 140–154.

(55) Walker, R. Temperature Coefficients for Reactions of OH Radicals with Alkanes between 300 and 1000 K. *Int. J. Chem. Kinet.* **1985**, 17, 573–582.

- (56) Gulati, S. K.; Walker, R. W. Arrhenius Parameters for the Reaction  $iC_3H_7+O_2-C_3H_{6+}HO_2$ . *J. Chem. Soc., Faraday Trans.* 2 **1988**, 84, 401–407.
- (57) Bronsted, J. Acid and Basic Catalysis. Chem. Rev. 1928, 5, 231–338.
- (58) Evans, M.; Polanyi, M. Inertia and Driving Force of Chemical Reactions. *Trans. Faraday Soc.* **1938**, *34*, 11–24.
- (59) Kropp, T.; Mavrikakis, M. Brønsted-Evans-Polanyi Relation for CO Oxidation on Metal Oxides Following the Mars—van Krevelen Mechanism. *J. Catal.* **2019**, 377, 577—581.
- (60) Kwon, S.; Deshlahra, P.; Iglesia, E. Dioxygen Activation Routes in Mars-van Krevelen Redox Cycles Catalyzed by Metal Oxides. *J. Catal.* **2018**, 364, 228–247.
- (61) Kwon, S.; Deshlahra, P.; Iglesia, E. Reactivity and Selectivity Descriptors of Dioxygen Activation Routes on Metal Oxides. *J. Catal.* **2019**, 377, 692–710.
- (62) Siders, P.; Marcus, R. Quantum Effects for Electron-Transfer Reactions in the "Inverted Region. *J. Am. Chem. Soc.* **1981**, *103*, 748–752.
- (63) Hammond, G. S. A Correlation of Reaction Rates. *J. Am. Chem. Soc.* **1955**, *77*, 334–338.
- (64) Chan, W. H.; Nordstrom, R. J.; Galvert, J. G.; Shaw, J. H. An IRFTS Spectroscopic Study of the Kinetics and the Mechanism of the Reactions in the Gaseous System, HONO, NO, NO<sub>2</sub>, H<sub>2</sub>O. *Chem. Phys. Lett.* **1976**, *37*, 441–446.
- (65) Kim, S.-K.; Kang, H. Efficient Conversion of Nitrogen Dioxide into Nitrous Acid on Ice Surfaces. *J. Phys. Chem. Lett.* **2010**, *1*, 3085–3089.
- (66) Chou, A.; Zhiru; Tao, F.-M. Density Functional Studies of the Formation of Nitrous Acid from the Reaction of Nitrogen Dioxide and Water Vapor. *J. Phys. Chem. A* **1999**, *103*, 7848–7855.
- (67) Deshlahra, P.; Carr, R. T.; Chai, S.-H.; Iglesia, E. Mechanistic Details and Reactivity Descriptors in Oxidation and Acid Catalysis of Methanol. *ACS Catal.* **2015**, *5*, 666–682.
- (68) Khodakov, A.; Yang, J.; Su, S.; Iglesia, E.; Bell, A. T. Structure and Properties of Vanadium Oxide-Zirconia Catalysts for Propane Oxidative Dehydrogenation. *J. Catal.* **1998**, *177*, 343–351.
- (69) Miller, J. A.; Klippenstein, S. J. Dissociation of Propyl Radicals and Other Reactions on a C<sub>3</sub>H<sub>7</sub> Potential. *J. Phys. Chem. A* **2013**, *117*, 2718–2727
- (70) Slagle, I. R.; Park, J.-Y.; Gutman, D. Experimental Investigation of the Kinetics and Mechanism of the Reaction of n-Propyl Radicals with Molecular Oxygen from 297 to 635 K. *Symp. (Int.) Combust., [Proc.]* **1985**, 20, 733–741.
- (71) Tian, J.; Tan, J.; Xu, M.; Zhang, Z.; Wan, S.; Wang, S.; Lin, J.; Wang, Y. Propane Oxidative Dehydrogenation over Highly Selective Hexagonal Boron Nitride Catalysts: The Role of Oxidative Coupling of Methyl. *Sci. Adv.* **2019**, *5*, No. eaav8063.
- (72) Annamalai, L.; Liu, Y.; Ezenwa, S.; Dang, Y.; Suib, S. L.; Deshlahra, P. Influence of Tight Confinement on Selective Oxidative Dehydrogenation of Ethane on MoVTeNb Mixed Oxides. *ACS Catal.* **2018**, *8*, 7051–7067.
- (73) Stern, D. L.; Grasselli, R. K. Reaction Network and Kinetics of Propane Oxydehydrogenation over Nickel Cobalt Molybdate. *J. Catal.* **1997**, *167*, 560–569.
- (74) Frank, B.; Dinse, A.; Ovsitser, O.; Kondratenko, E. V.; Schomäcker, R. Mass and Heat Transfer Effects on the Oxidative Dehydrogenation of Propane (ODP) over a Low Loaded VO<sub>x</sub>/Al<sub>2</sub>O<sub>3</sub> Catalyst. *Appl. Catal., A* **2007**, 323, 66–76.
- (75) Dinse, A.; Khennache, S.; Frank, B.; Hess, C.; Herbert, R.; Wrabetz, S.; Schlögl, R.; Schomäcker, R. Oxidative Dehydrogenation of Propane on Silica (SBA-15) Supported Vanadia Catalysts: A Kinetic Investigation. J. Mol. Catal. A: Chem. 2009, 307, 43–50.
- (76) Liu, J.; Mohamed, F.; Sauer, J. Selective Oxidation of Propene by Vanadium Oxide Monomers Supported on Silica. *J. Catal.* **2014**, *317*, 75–82.

(77) Pitzer, L.; Sandfort, F.; Strieth-Kalthoff, F.; Glorius, F. Intermolecular Radical Addition to Carbonyls Enabled by Visible Light Photoredox Initiated Hole Catalysis. *J. Am. Chem. Soc.* **2017**, *139*, 13652–13655.

- (78) Sahoo, B.; Hopkinson, M. N.; Glorius, F. Combining Gold and Photoredox Catalysis: Visible Light-Mediated Oxy- and Aminoarylation of Alkenes. *J. Am. Chem. Soc.* **2013**, *135*, 5505–5508.
- (79) Jia, K.; Zhang, F.; Huang, H.; Chen, Y. Visible-Light-Induced Alkoxyl Radical Generation Enables Selective C (sp<sup>3</sup>)–C (sp<sup>3</sup>) Bond Cleavage and Functionalizations. *J. Am. Chem. Soc.* **2016**, *138*, 1514–1517
- (80) Xie, J.; Shi, S.; Zhang, T.; Mehrkens, N.; Rudolph, M.; Hashmi, A. S. K. A Highly Efficient Gold-Catalyzed Photoredox  $\alpha$ -C (sp³)-H Alkynylation of Tertiary Aliphatic Amines with Sunlight. *Angew. Chem., Int. Ed.* **2015**, *54*, 6046–6050.
- (81) Towns, J.; Cockerill, T.; Dahan, M.; Foster, I.; Gaither, K.; Grimshaw, A.; Hazlewood, V.; Lathrop, S.; Lifka, D.; Peterson, G. D.; et al. XSEDE: Accelerating Scientific Discovery. *Comput. Sci. Eng.* **2014**, *16*, *62*–74.